The Egyptian Journal of Remote Sensing and Space Sciences 29 (2026) 742–766

Contents lists available at ScienceDirect

The Egyptian Journal of Remote Sensing and Space Sciences

journal homepage: www.sciencedirect.com

Research Paper

Deciphering Precambrian Litho-structural settings and barite-associated mineralization through integrated hyperspectral and geophysical datasets

Abazar M.A. Daoud [a,b,*], Ali A. Mohieldain [c,1], Albarra Satti [b], Ali Shebl [a,d], Richard W. McIntosh [a], Árpad Csámer [a,e], Péter Rózsa [a]

[a] Department of Mineralogy and Geology, University of Debrecen, 4032 Egyetem tér 1., Debrecen, Hungary.
[b] Faculty of Earth Sciences, Red Sea University, Red Sea State, Port Sudan, Sudan
[c] Exploration Geosciences Institute, University of Miskolc, Egyetem út 1, Miskolc-Egyetemváros, 3515, Hungary
[d] Department of Geology, Tanta University, Tanta, 31527, Egypt
[e] Cosmochemistry and Cosmic Methods Research Group, University of Debrecen, Debrecen, 4032, Hungary

ARTICLE INFO

Keywords:
Remote sensing
Machine learning
Hyperspectral imaging
Lithological mapping
Gravity analysis
Arabian–Nubian Shield
PRecursore IperSpettrale della Missione Applicativa (PRISMA)
Barite exploration

ABSTRACT

Effective lithological mapping and mineral exploration remain challenging in geologically complex and underexplored Precambrian terrains. This is particularly relevant to the Arabian–Nubian Shield (ANS), a Neoproterozoic orogenic belt extending across northeastern Africa and Arabia. This study integrates Landsat 8/9, Sentinel-2, ASTER, PRecursore IperSpettrale della Missione Applicativa (PRISMA) hyperspectral imagery, gravity-derived structural analysis, supervised machine learning, and field observations to characterize lithology, alteration, and structural controls relevant to barite exploration in the Tehilla–Abu Samar area, Red Sea Hills, northeastern Sudan. Band ratios, principal component analysis, false-colour composites, Minimum Noise Fraction transformation, and Sequential Maximum Angle Convex Cone analysis were used to enhance lithological and mineral-sensitive spectral variations. Five classifiers—support vector machine (SVM), artificial neural network, random forest, k-nearest neighbors, and eXtreme Gradient Boosting (XGBoost)—were evaluated for lithological classification. XGBoost achieved the highest overall accuracy (81.49%) and Kappa coefficient (0.792), closely followed by SVM (81.40%; $\kappa = 0.791$), while SVM yielded a marginally higher macro-F1 score. Gravity anomaly and edge-enhancement analyses delineated major NE–SW and NW–SE structural trends and density contrasts associated with intrusive bodies and deformation zones. Integration of independently derived lithological, spectral, structural, and field evidence established felsic metavolcanic rocks as the principal barite-hosting lithology and provided a coherent framework for prioritizing barite-associated geological targets in this structurally complex Precambrian terrane.

1. Introduction

Lithological mapping in Precambrian terranes characterized by intense deformation, hydrothermal alteration, and magmatic overprinting remains challenging, particularly in arid and underexplored regions where field accessibility is limited. In the Arabian–Nubian Shield (ANS), the close spatial association of volcanic, plutonic, metamorphic, and altered rock units commonly leads to ambiguity in conventional geological mapping and mineral exploration (Abdelkareem et al., 2024; Abo Khashaba et al., 2026; Elfadly et al., 2026; Younis et al., 2025). These challenges are especially pronounced in the Red Sea Hills (RSH) of northeastern Sudan, a region known for its complex Precambrian lithologies and significant metallic and industrial mineral potential.

Barite mineralization in the RSH is commonly associated with Neoproterozoic volcanic, intrusive, and structurally controlled hydrothermal systems (Abu-Fatima et al., 2021; Daoud et al., 2025; Elsamani et al., 2001; Satti et al., 2026). In the Tehilla–Abu Samar area, barite-bearing lithologies occur alongside granitoids, gabbroic intrusions, metavolcanic–metasedimentary sequences, and major shear zones, forming a geologically complex exploration environment. However, the spatial distribution of these lithologies and their structural relationships remain insufficiently constrained because of limited exposure, rugged

* Corresponding author at: Department of Mineralogy and Geology, University of Debrecen, 4032 Egyetem tér 1, Debrecen, Hungary
E-mail address: Abazar.daoud@science.unideb.hu (A.M.A. Daoud).
[1] 0009-0004-6189-7226

https://doi.org/10.1016/j.ejrs.2026.10.001
Received 22 June 2026; Received in revised form 8 September 2026; Accepted 4 October 2026
Available online 14 October 2026
1110-9823/© 2026 Published by Elsevier B.V. on behalf of National Authority of Remote Sensing & Space Science. This is an open access article under the CC BY-NC-ND license (http://creativecommons.org/licenses/by-nc-nd/4.0/).

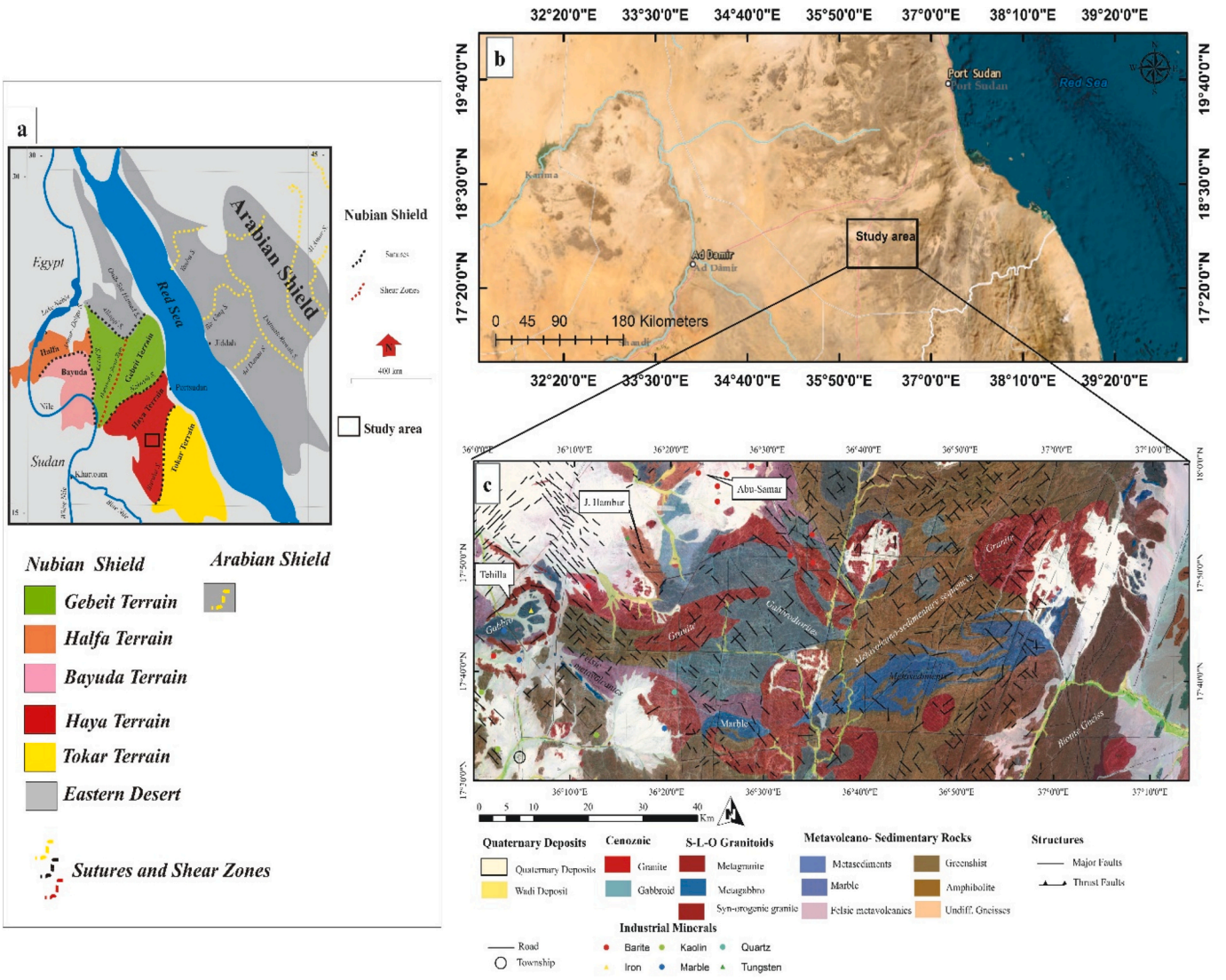


Fig. 1. (a) Regional location of the study area within the Sudanese part of the ANS; (b) location of the Tehilla–Abu Samar area near Derudeb; and (c) detailed geological map showing the principal lithostratigraphic and structural units, including presumed pre-Pan-African high-grade metamorphic basement (ca. 2500–1000 Ma), Neoproterozoic metavolcano-sedimentary sequences (ca. 900–800 Ma), *syn*- to late-orogenic intrusive assemblages (ca. 815–724 Ma), post-orogenic granitoid and gabbroic intrusions (ca. 720–550 Ma), the Lower Paleozoic TRC, Nubian Supergroup sedimentary rocks (Early Paleozoic–Cretaceous), Red Sea rift-related volcanics (ca. 31–22 Ma), and Quaternary deposits. Geological framework modified after Kenea H Nasir (1997). (For interpretation of the references to colour in this figure legend, the reader is referred to the web version of this article.)

Table 1
Simplified lithostratigraphic framework of the Tehilla–Abu Samar study area and associated age constraints (Abdel Rahman, 1993; Kenea et al., 2001; Semtner and Klitzsch, 1994; Shackleton, 1994; Vail, 1988).

Geological unit	Principal lithologies	Approximate age	Tectono-stratigraphic significance
Quaternary deposits	Alluvial, aeolian, and wadi sediments	Quaternary–Recent	Unconsolidated surficial deposits
Red Sea rift-related volcanics	Basalt, rhyolite, dacite and quartz porphyry	ca. 31–22 Ma	Volcanism associated with Red Sea rifting
Nubian Supergroup	Sandstone, siltstone, mudstone, limestone and conglomerate	Early Paleozoic–Cretaceous	Post-basement sedimentary cover
Tehilla Ring Complex (TRC)	Troctolite, norite, granite and associated basic–felsic intrusive rocks	Lower Paleozoic	Post-tectonic alkaline ring-complex magmatism
Post-orogenic intrusive assemblage	Granite and gabbroic rocks	ca. 720–550 Ma	Late- to post-orogenic magmatism
Syn- to late-orogenic intrusive assemblage	Meta-granite, meta-granodiorite, metagabbro and associated mafic–ultramafic rocks	ca. 815–724 Ma	Pan-African *syn*- to late-orogenic magmatism
Metavolcano-sedimentary sequence	Schist, marble, metaconglomerate, metapelite, metarhyolite, meta-andesite and metatuff	ca. 900–800 Ma	Pan-African arc/back-arc volcano-sedimentary succession
High-grade metamorphic basement	Gneiss, amphibolite, quartzite and migmatitic rocks	ca. 2500–1000 Ma	Presumed pre-Pan-African crustal segment

topography, and the heterogeneity of surface spectral responses.

Recent studies demonstrate the increasing application of multisensor

Table 2
Remote-sensing datasets and acquisition characteristics used in this study.

Dataset	Acquisition date (s)	Product level	Spectral Range	Swath Width	Spectral characteristics	Native spatial resolution
Landsat 8/9 OLI–TIRS / OLI-2–TIRS-2	29 Sep 2023 (L8); 6 Mar 2024 (L9)	Collection 2 Level-1 Precision Terrain Corrected (L1TP), Tier 1	0.43–12.51 μm (VNIR, SWIR, TIR)	185 km	11 bands; VNIR–SWIR–TIR.	15 m Pan; 30 m multispectral; 100 m native TIR
Sentinel-2 A MSI	11 Oct 2023; 30 Nov 2023	Level-2 A (11 Oct 2023); Level-1C (30 Nov 2023)	0.443–2.19 μm (VNIR–SWIR)	290 km	13 bands; VNIR–red edge–SWIR.	10, 20 and 60 m
ASTER	26 Feb 2006; 8 Oct 2006	ASTER Level-1 Precision Terrain Corrected Registered At-Sensor Radiance (AST_L1T)	0.52–11.65 μm.	60 km	14 VNIR–SWIR–TIR bands, 15/ 30/90 m	15 m VNIR; 30 m SWIR; 90 m TIR
PRISMA	26 January 2023	Level-2D Standard (L2D STD)	0.4–2.5 μm (VNIR, SWIR, hyperspectral)	30 km	240 hyperspectral bands (66 VNIR +174 SWIR), 1 panchromatic band	30 m hyperspectral; 5 m Pan

Abbreviations: VNIR, visible and near-infrared; SWIR, shortwave infrared; TIR, thermal infrared; MS, multispectral; HS, hyperspectral; Pan, panchromatic.

Table 3
Sensor-specific band ratios and spectral indices used for lithological and alteration-related mapping.

Spectral target	L8/9	S2	ASTER	PRISMA	Geological interpretation
Ferric-oxide response	B4/B3	B4/B3	B4/B2	(B44 + B62)/B57	Enhancement of Fe^{3+}-bearing, oxidized surfaces
(Heller Pearlshtien et al., 2021; Van der Meer et al., 2014; van der Werff and van der Meer, 2015)					
Ferrous-iron response	B4/B6	B4/B11 B2/B4		B20/B9	Enhancement of Fe^{2+}-bearing and alteration-related surfaces
(Abrams and Yamaguchi, 2019; van der Werff and van der Meer, 2015)					
OH-bearing alteration	B6/B7	B11/B12	B4/B5	(B125 + B136)/B133; B66/ (B126 + B45)	Hydroxyl-bearing alteration zones
(Chirico et al., 2023; Kokaly et al., 2017)					
Silica−/lithology-sensitive response	B5/B7	B12/B11	B5/B4	(B149 + B154)/B152; (B140/ B50) × (B30/B20) (This study)	Enhancement of siliceous and lithologically contrasting surfaces
(Ninomiya and Fu, 2019; Pour et al., 2019; Van der Meer et al., 2014)					
Carbonate-sensitive response	(B5 + B7)/B6	B12/B2	(B6 + B9)/B8	(B149 + B154)/B152	Discrimination of carbonate-rich units, including marble
(Kokaly et al., 2017; Ninomiya and Fu, 2019; Rockwell and Hofstra, 2008)					
Barite-associated spectral response	(B6/ B7) − (B5/B4)	B11/B2	B5/B4	PC5; MNF5 (This study)	Enhancement of spectral responses spatially associated with barite-bearing lithologies
(Daoud et al., 2025; Madani and Emam, 2011; Rockwell and Hofstra, 2008)					
Sulfide−/alteration-associated response	B7/B6	B12/B2 or B6/B8A	(B4 + B6)/B5	MNF5 (This study)	Enhancement of alteration patterns potentially associated with sulfide-bearing zones
(Kokaly et al., 2017; Rockwell et al., 2021; Rockwell and Hofstra, 2008)					
Sulfate−/barite-associated response	(B2/ B1) − (B5/B4)	B11/B8A	(B10 × B12)/($B11^2$); (B5 + B7)/B6	IC9 (This study)	Enhancement of sulfate-sensitive responses associated with barite-bearing settings
(Daoud et al., 2025; Madani and Emam, 2011; Rockwell and Hofstra, 2008)					
Iron-oxide-sensitive response B6/B7 or B4/B2 B4/B2			B4/B2	(B143 + B144)/(B133 + B134)	Combined iron-oxide/alteration response
(Askari et al., 2018; Pour et al., 2019)					
Lateritic/ferruginous response	B6/B7	B11/B12	B5/B4	(B44 + B62)/B57	Enhancement of lateritic and ferruginous surfaces
(Chirico et al., 2023; Van der Meer et al., 2014)					
Kaolinite−/clay-sensitive response	B7/B6	B7/B6	B7/B5	B66/(B126 + B45)	Enhancement of kaolinite- and clay-bearing alteration
(Bishop et al., 2018; Rowan and Mars, 2003; Tripathi and Garg, 2020)					
Gossan/ferruginous alteration	B6/B4	B11/B4	B4/B2	B30/B20	Delineation of gossanous and strongly oxidized surfaces
(Pour et al., 2019; Van der Meer et al., 2012)					

remote sensing and machine-learning (ML) techniques to lithological mapping and mineral exploration in complex basement terranes (Abo Khashaba et al., 2026; Asghede et al., 2025; Daoud et al., 2025; Younis et al., 2025). Multispectral datasets such as Landsat (L8/9), Sentinel-2 (S2), and Advanced Spaceborne Thermal Emission and Reflection Radiometer (ASTER) have been widely used to discriminate lithologies and identify alteration-related spectral signatures, while hyperspectral imagery provides better spectral features for mineralogical characterization (Ali-Bik et al., 2025; Ghoneim et al., 2023). Arian et al. (2025), for example, integrated ASTER and Sentinel-2 imagery to map potential lithium-bearing pegmatite zones, while Mahboob et al. (2024) demonstrated the use of satellite remote sensing and ML for predictive mineral prospectivity modeling. Recent studies demonstrate the increasing importance of integrating complementary spectral information with data-driven methods to enhance geological discrimination and exploration targeting. They also emphasize the necessity of clearly differentiating lithological classification, mineral-sensitive spectral mapping, and predictive mineral prospectivity modeling (Abdelkareem et al., 2024; Shebl et al., 2024; Younis et al., 2025).

Previous investigations in the RSH have primarily utilized multispectral remote sensing, conventional image-processing techniques, or remote sensing in combination with individual geophysical datasets (Daoud et al., 2025; Ibrahim et al., 2016; Mina et al., 2025; Mohamed Taha et al., 2024; Satti et al., 2026). In contrast, the combined use of multispectral imagery, hyperspectral data, supervised lithological classification, gravity-derived structural analysis, and field observations has

Table 4
Machine-learning classifiers, final parameter settings, and computational environment used for lithological classification.

Model	Final parameter settings	Platform
SVM	RBF kernel; γ = 0.333; C = 100; one-vs-one multiclass classification; standardized features	ENVI
ANN	Training threshold = 0.9; training rate = 0.2; momentum = 0.9; RMS exit criterion = 0.1; hidden layers = 1; iterations = 1000	
RF	max_features = 2; min_samples_leaf = 5; bootstrap ensemble, Trees = 500.	Python/Google Colab and R/ RStudio
XGB	max_depth = 6; learning_rate = 0.05; min_child_weight = 5; n_estimators = 200; subsample = 0.8; colsample_bytree = 1.0; gamma = 0	
KNN	k = 7; Euclidean distance; standardized predictors	

been infrequently explored in the Tehilla–Abu Samar area. The present study integrates these independent datasets within a unified geological framework to assess lithological distribution, mineral-sensitive spectral responses, subsurface density contrasts, and structural controls relevant to barite exploration. ML algorithms classify lithological units, while multispectral and hyperspectral analyses characterize lithological and mineral-sensitive spectral responses. Gravity-derived products are utilized to delineate subsurface structures and lithological boundaries. This study therefore integrates independently derived results to assess barite occurrences, their host lithologies, and associated spectral and structural anomalies.

Within this framework, three questions are addressed: (1) To what extent do complementary multispectral and PRISMA hyperspectral observations enhance the discrimination of principal lithological units and mineral-sensitive spectral responses in the Tehilla–Abu Samar area? (2) How do different ML algorithms perform in distinguishing lithologies characterized by heterogeneous and partially overlapping spectral signatures? (3) In what ways do gravity-derived structural features complement surface lithological and spectral information in constraining the geological setting of documented and prospective barite-associated zones? The central hypothesis posits that integrating independent spectral, lithological, structural, and field constraints yields a more coherent characterization of the geological framework than interpreting individual datasets. Additionally, classification performance is expected to vary according to lithological heterogeneity and spectral separability.

Table 5
Distribution of training and testing samples (point pixel) for lithological classification in the study area.

Lithology	Representative verified field check			Training points	Validation points
	North	East	Field stations		
Younger granite	17°42′39.13”	36° 5′20.44”	2	1639	450
Gabbro	17°45′44.59”	36° 5′41.81”	3	1488	442
Felsic metavolcanics	18° 4′56.70”	36°15′27.94”	2	1695	499
Metasediments (Marble)	17°41′56.68”	36° 4′50.87”	3	1032	296
Granodiorite	17°50′10.39”	36°23′25.23”	1	1320	390
Greenschist facies	17°43′29.57”	36°14′42.52”	4	1008	319
Syn to Late granite	17°39′14.47”	36°27′13.91”	3	816	240
Quaternary deposits	17°53′10.15”	36° 9′16.21”	5	1451	419
Wadi deposits	17°45′24.65”	36° 2′32.58”	2	1616	469
Rhyolite body	17°46′44.64”	36°10′57.94”	1	318	95
Total	–	–	26	12,383	3619

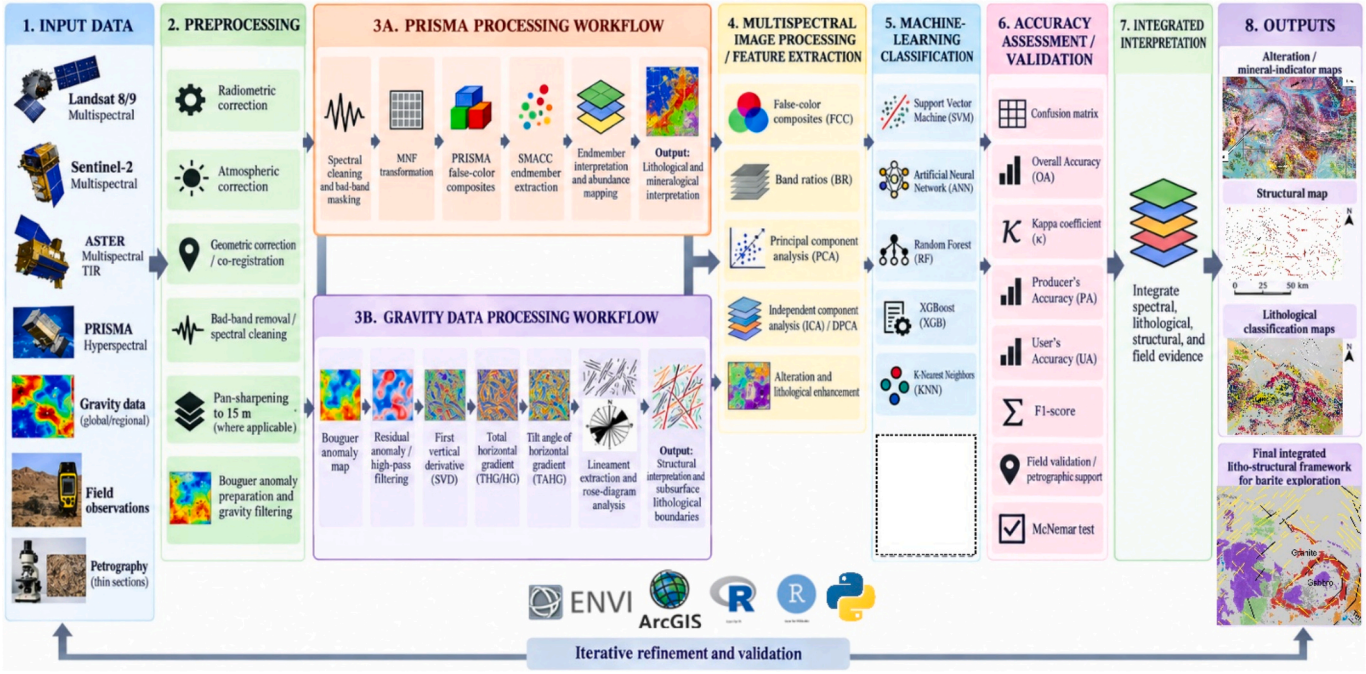


Fig. 2. Flowchart illustrating the methodology used in the present study.

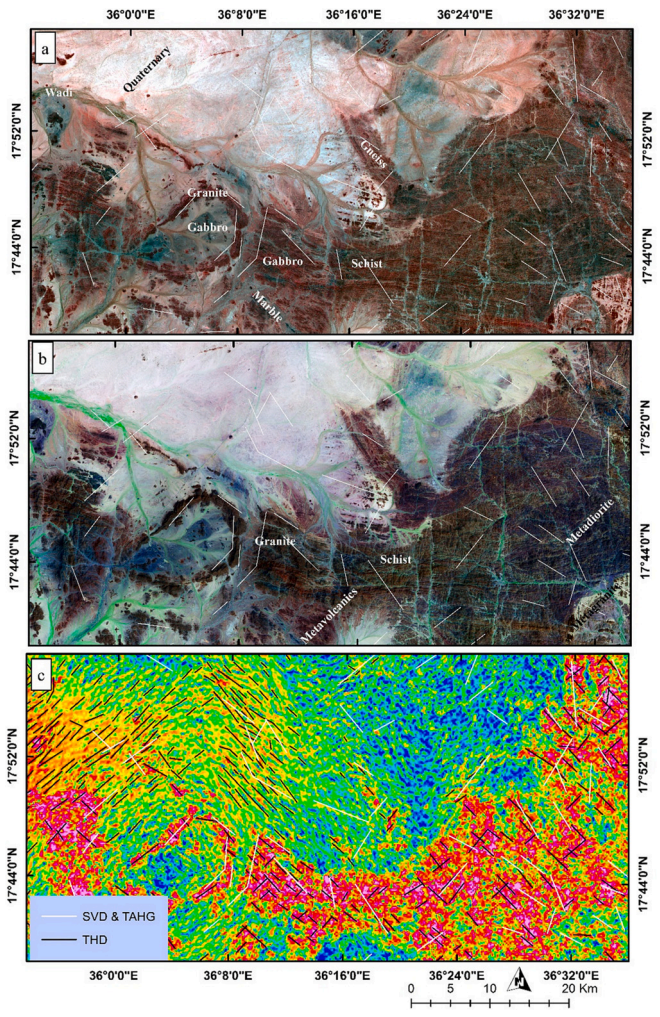


Fig. 3. (a) False colour composites of S2 (R12–G–B1), (b) ASTER (R5–G2–B1) images, (c) the TAHG gravity map emphasizing subsurface lineaments and density contrasts.

2. Study area and geological setting

The Tehilla–Abu Samar study area is located near Derudeb in the southwestern RSH, northeastern Sudan, within the Sudanese sector of the ANS (Figs. 1a-c). It extends between approximately 17°32′–18°07′ N and 35°53′–37°00′ E and encompasses the Tehilla Ring Complex (TRC), Abu Samar, Derudeb, and adjacent Precambrian basement terrains.

Regionally, the Sudanese Nubian Shield is subdivided into several Neoproterozoic juvenile crustal terranes, commonly recognized from north to south as the Gerf, Gabgaba, Gebeit, Haya, and Tokar terranes (Fig. 1a). These terranes were progressively assembled during the Pan-African orogeny and are separated by major shear zones and ophiolite-bearing sutures that record the amalgamation of juvenile island-arc and back-arc crust (Abdelsalam and Stern, 1996; Johnson et al., 2003; Stern and Abdelsalam, 1998). The Nakasib Suture forms an important tectonic boundary between the Gebeit Terrane to the north and the Haya Terrane to the south and records Neoproterozoic terrane collision and subsequent deformation (Abdelsalam and Stern, 1996; Adam et al., 2024; Johnson et al., 2013; Stern et al., 2004; Wipfler, 1996).

The Tehilla–Abu Samar area lies within the Haya Terrane and is affected by major Pan-African structural systems, particularly the Amur–Nakasib suture system and the Tehilla shear zone (Fig. 1b). The Haya Terrane comprises part of the juvenile Neoproterozoic crust of the ANS and records volcanic-arc development, ophiolite emplacement, granitoid magmatism, metamorphism, deformation, and later tectonic reworking (Abdelsalam and Stern, 1996; Adam et al., 2024; Ahmed, 1977; Johnson et al., 2013; Kenea et al., 2001).

The lithostratigraphic succession records an extended geological evolution from recognized pre-Pan-African basement rocks to Cenozoic volcanism and Quaternary sedimentation. The oldest exposed units comprise high-grade gneissic and migmatitic rocks, locally interpreted as a pre-Pan-African crustal component (Abdel Rahman, 1993; Abdelsalam and Stern, 1993; Kröner and Stern, 2004). These are associated with Neoproterozoic metavolcano-sedimentary sequences comprising schist, marble, metaconglomerate, metapelite, metarhyolite, meta-andesite, and metatuff, broadly related to Pan-African arc and back-arc evolution (Abdel Rahman, 1993; Kenea et al., 2001). Syn- to late-orogenic intrusive assemblages were emplaced mainly during ca. 815–724 Ma, followed by post-orogenic granitoid and gabbroic magmatism (Kenea H Nasir, 1997; Shackleton, 1994). The principal lithostratigraphic units and their age relationships are summarized in Table 1.

The TRC is an approximately 8–11 km diameter alkaline intrusive complex composed of successive mafic and felsic phases (Ahmed, 1977; Sadig and Ahmed, 1989; Shang et al., 2010; Vail, 1985). The early mafic phase comprises principally mafic intrusive rocks emplaced as lopolith- and sill-like bodies, whereas the later felsic phase is dominated by granitic intrusions and associated cone-sheet structures. The adjacent Abu Samar area contains ophiolitic mafic–ultramafic rocks, massive basalt, and dolerite associated with quartzite, silicified barite, manganese mineralization, and iron-rich gossans (Elsamani et al., 2001; Kenea et al., 2001; Satti et al., 2026). Marble and other metavolcano-sedimentary rocks occur particularly south of the TRC and along the Tehilla structural zone, while granitoids and gabbroic bodies are widespread around the complex. These Precambrian and Paleozoic basement assemblages are unconformably overlain by sedimentary successions of the Nubian Supergroup and subsequently by Red Sea rift-related volcanic rocks and Quaternary superficial deposits (see Fig. 1c).

Structurally, the study area records polyphase deformation expressed by folds, shear zones, faults, fractures, and intrusive contacts. Regional structural fabrics are dominated by NE–SW to NNE–SSW and NW–SE trends, including the Tehilla shear zone and associated secondary structures around the TRC (See Appendix A) (Abdel Rahman, 1993; Abdelsalam, 2010; Bosworth and Stockli, 2016; Stern and Johnson, 2018). This litho-structural complexity provides a practical testbed for evaluating the integration of multisource features and machine-learning-based litho-structural mapping.

3. Materials and methods

3.1. Remote sensing data and preprocessing

3.1.1. Multispectral and hyperspectral datasets and preprocessing

L8/9, S2, ASTER, and PRISMA imagery were used for lithological and mineral-sensitive spectral analysis. Only cloud-free scenes were selected (0.0%). Acquisition dates, product levels, spectral characteristics, and native spatial resolutions are summarized in Table 2.

For L8/9, S2, and ASTER, the reflective visible and near-infrared to shortwave infrared (VNIR–SWIR) data were radiometrically calibrated, where required, and atmospherically corrected to surface reflectance using the FLAASH module in ENVI v.5.3 (Cooley et al., 2002). ASTER thermal infrared bands were retained as calibrated thermal data and were not subjected to the correction. The corrected datasets were subsequently co-registered and prepared for spectral enhancement and geological interpretation in ENVI and ArcGIS 10.5. For Landsat-based lithological classification, the 30 m multispectral bands were pan-sharpened to a 15 m output grid using the panchromatic Band 8 through the standard pan-sharpening procedure in ArcGIS.

As the PRISMA Level-2D product is provided as atmospherically corrected and geocoded surface reflectance, no additional FLAASH correction was applied. Preprocessing included removal of noisy bands

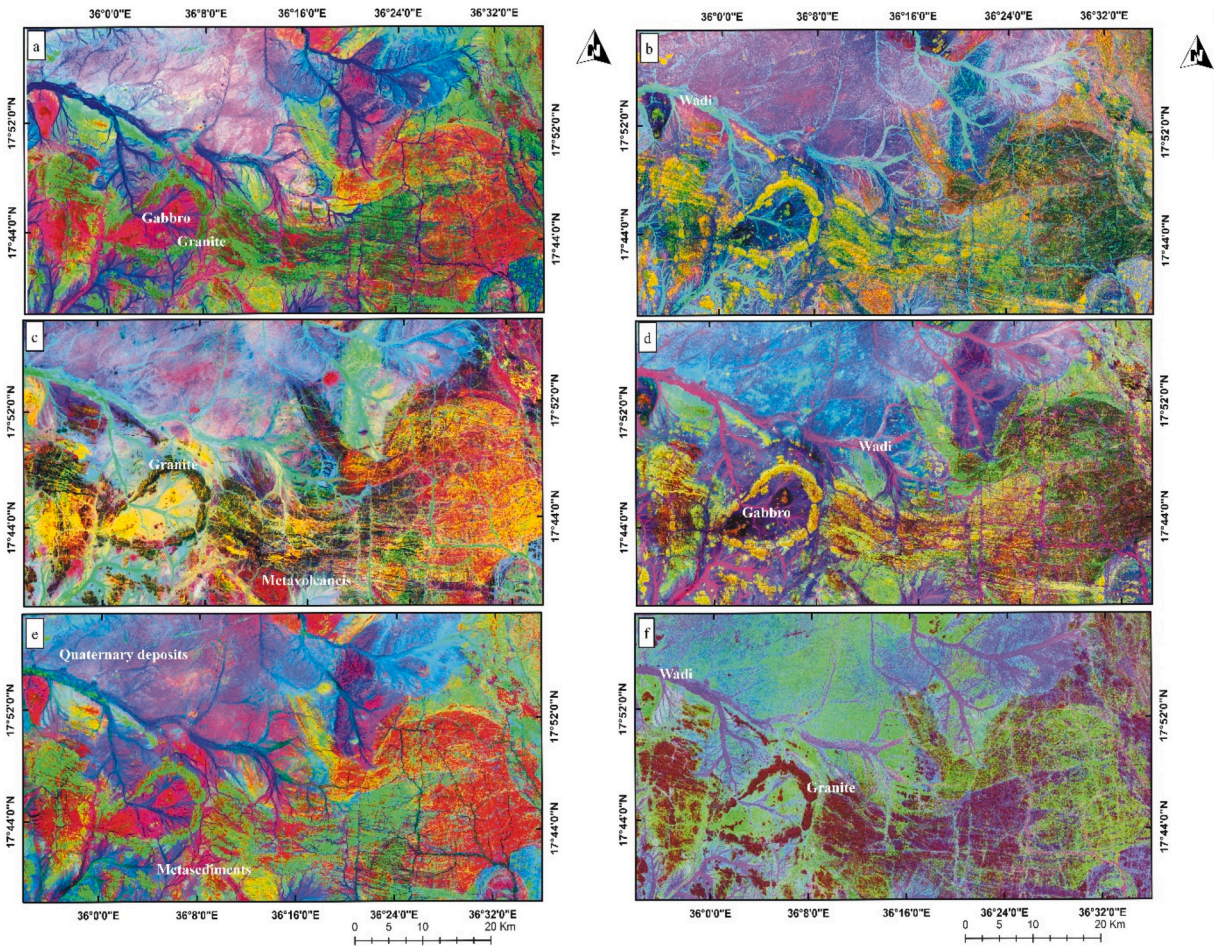


Fig. 4. Discrimination of lithology across the study area, (a) PC 7–5-3, (b) PC of bands 6–3-1, (c) R6/7–5/4-G5/6-B4/2, (d) PC of bands B5/B4, B7/B5, and B4/B2 in RGB delineating barite-associated high-response zones in light yellow, (e) R6/4-G4/3-B4/5 displaying gabbroic rocks in dark red and granitic rocks in green, metadiorites in light red, (f) PCA of iron-bearing minerals delineating felsic rocks in dark brown from mafic rocks in green. (For interpretation of the references to colour in this figure legend, the reader is referred to the web version of this article.)

and spectral regions affected by strong atmospheric water absorption prior to analysis. The cleaned hyperspectral cube was transformed using the Minimum Noise Fraction (MNF) method (Green et al., 1988), followed by Sequential Maximum Angle Convex Cone (SMACC) endmember extraction (Gruninger et al., 2004). PRISMA, ASTER, and the other spectral products were analyzed independently and were not combined into a single machine-learning predictor stack; their derived information was subsequently integrated during geological interpretation.

3.1.2. *Spectral enhancement and feature extraction*

False-colour composites (FCCs) were generated from the atmospherically corrected reflectance data using sensor-specific band combinations selected to enhance lithological contrast. Principal Component Analysis (PCA) and Independent Component Analysis (ICA) were applied to the multispectral datasets to reduce spectral redundancy and emphasize lithologically significant variance (Maćkiewicz and Ratajczak, 1993), whereas MNF transformation was applied to the PRISMA hyperspectral dataset to separate coherent spectral information from residual noise (Esmaeili et al., 2024; Harris et al., 2005; Shebl et al., 2024; Sorrentino et al., 2024).

Band-ratio (BR) analysis was performed on the corrected reflectance data to enhance spectral responses associated with ferric and ferrous iron, hydroxyl-bearing phases, carbonates, silica-rich materials, sulfates, and other alteration-related surface materials (Askari et al., 2018; Pour et al., 2023; Van der Meer et al., 2014, 2012; van der Werff and van der Meer, 2015). Because equivalent band numbers correspond to different wavelength intervals among L8/9, S2, ASTER, and PRISMA, the sensor-specific ratios, formulas, spectral targets, and geological applications used in this study are summarized in Table 3.

3.1.3. *PRISMA hyperspectral processing and endmember analysis*

The spectrally cleaned PRISMA reflectance cube was subjected to Minimum Noise Fraction (MNF) transformation to suppress residual noise and concentrate coherent spectral information into a reduced number of components (Green et al., 1988; Habashi et al., 2024; Harris et al., 2005; Shebl et al., 2024). MNF components 4, 5, and 6 were selected for RGB visualization because they provided the clearest lithological contrast among the principal units during image inspection. A PRISMA composite using bands 190, 187, and 140 was also generated to examine spectral variability associated with mapped lithological units and documented barite occurrences. These bands were selected empirically from the processed cube based on their ability to enhance contrast between the prinispal host rocks and adjacent lithologies; they are therefore used as a visualization product rather than as a diagnostic barite index.

Endmember extraction was performed using the SMACC algorithm (Aggarwal and Garg, 2015; Gruninger et al., 2004). The extracted VNIR–SWIR spectra were interpreted according to the position, shape, and relative depth of diagnostic absorption features and were compared with reference mineral spectra from the USGS Spectral Library. Geological-map information and field observations were used as

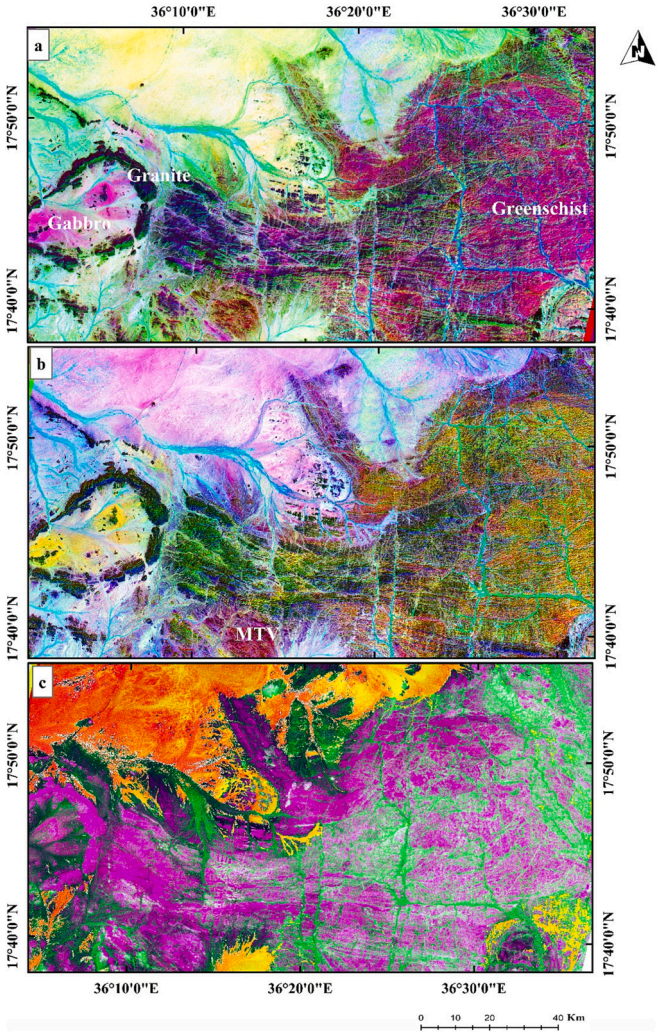


Fig. 5. ASTER lithological discrimination (a) MNF of bands 1, 2, 3 in RGB discriminating granitoids in green, (b) B4/B7-B5/B4-PC1 delineate gabbro in yellow and metavolcanics in red, (c) ferric (red) ferrous (green) and clay minerals (yellow) in RGB respectively discriminating weathering products. (For interpretation of the references to colour in this figure legend, the reader is referred to the web version of this article.)

additional constraints during endmember assignment. No numerical spectral-similarity metric was applied; endmember assignment was based on the position, shape, and relative depth of diagnostic absorption features, comparison with USGS reference spectra, and geological/field constraints (Alawy et al., 2025; Orynbassarova et al., 2025). The resulting MNF products, spectral composites, endmember spectra, and abundance maps were interpreted independently of the supervised lithological classifiers and were subsequently integrated with multi-spectral, field, and structural information.

3.2. Geophysical data and structural feature extraction

3.2.1. Gravity data

Free satellite gravity data was obtained from the Global Gravity Model plus (GGMplus), a composite model integrating long-wavelength GOCE/GRACE satellite, intermediate-wavelength information from EGM2008, and short-wavelength topographic gravity derived from high-resolution terrain models (Camacho and Alvarez, 2021; Hirt et al., 2013). GGMplus is distributed on a nominal 7.2 arc-second grid, corresponding to approximately 200 m of north–south sampling within the study area. This grid spacing reflects the model's sampling interval rather than its geological resolving power, as most sub-kilometer signals originate from forward-modeled topographic gravity instead of direct observations of subsurface density variations to characterize regional, mesoscale gravity variations, and structural trends (Hirt et al., 2013).

The gravity dataset was processed to generate the Complete Bouguer Anomaly (CBA) and a residual anomaly field. A 10-km high-pass separation was applied to suppress broad regional wavelengths and emphasize comparatively shorter-wavelength gravity variations. The resulting CBA and residual products provided the basis for subsequent edge-enhancement and structural analysis (Abtout et al., 2018; Camacho and Alvarez, 2021; Chouhan, 2020; Clotilde et al., 2016).

3.2.2. Gravity filtering and structural interpretation

Structural analysis was based on complementary derivative filters applied to the gravity anomaly field. The Second Vertical Derivative (SVD) was used to enhance relatively short-wavelength gravity gradients and emphasize shallow density boundaries, whereas the Horizontal Gradient (HG) was applied to identify lateral gravity contrasts associated with lithological contacts and potential structural boundaries. The Tilt Angle of the Horizontal Gradient (TAHG) was additionally used to enhance both strong and comparatively subtle anomaly edges and to improve continuity of structural trends (Elkins, 1951; (Ferreira et al., 2013); Grauch and Cordell, 1987). The mathematical formulations of the SVD, HG, and TAHG filters are provided in Appendix A.

Lineaments were identified based on coherent linear or arcuate gradient maxima and discontinuities observed in the SVD, HG, and TAHG products. These features were then compared with mapped lithological contacts, remotely sensed lineaments, regional shear-zone orientations, and detailed field observations. Gravity-derived lineaments were treated as potential subsurface structural boundaries rather than direct fault indicators, and geological significance was assigned only when independent spatial or directional correspondence was established (Di Filippo et al., 2025; Hamimi et al., 2023; Pratama et al., 2023). Gravity-derived lineaments were manually digitized from coherent linear and arcuate gradient maxima and presented in rose diagrams that summarizes the orientations of the interpreted lineaments to assess dominant structural trends.

3.3. Machine learning framework for lithological mapping

Supervised machine-learning algorithms were applied to lithological classification using multispectral imagery. Five classifiers Extreme Gradient Boost (XGB), Support Vector Machine (SVM), Random Forest (RF), K-Nearest Neighbor (KNN), and Artificial Neural Network (ANN) were evaluated for discrimination of ten lithological classes due to their ability to model complex, nonlinear relationships among spectral predictors (Komadja et al., 2025; Serbouti et al., 2022). ASTER, PRISMA, and gravity-derived products were analyzed independently and were not included as machine-learning predictor variables. The mathematical formulations of the classifiers are provided in Appendix B, while their final parameter settings are summarized in Table 4.

A common reference dataset comprising 12,383 training and 3619 validation points was compiled from field observations, geological maps, and remote-sensing interpretation (Table 5). Sample numbers varied among lithological classes according to their spatial extent and exposure. The same reference dataset and validation locations were used for all five classifiers to document direct comparison. A coordinate-level overlap audit was additionally conducted to evaluate possible training–validation coincidence, with the strict sensitivity assessment reported in the Appendix.

SVM and ANN were implemented in ENVI (5.3), whereas RF, XGB, and KNN were implemented in Python within Google Colab and R language (R Core Team, 2021). The final classification raster was processed on a 15 m grid WGS84/UTM Zone 37 N (EPSG:32637). Model performance was evaluated using Overall Accuracy (OA), Cohen's Kappa coefficient (κ), Producer's Accuracy (PA), User's Accuracy (UA), and F1-

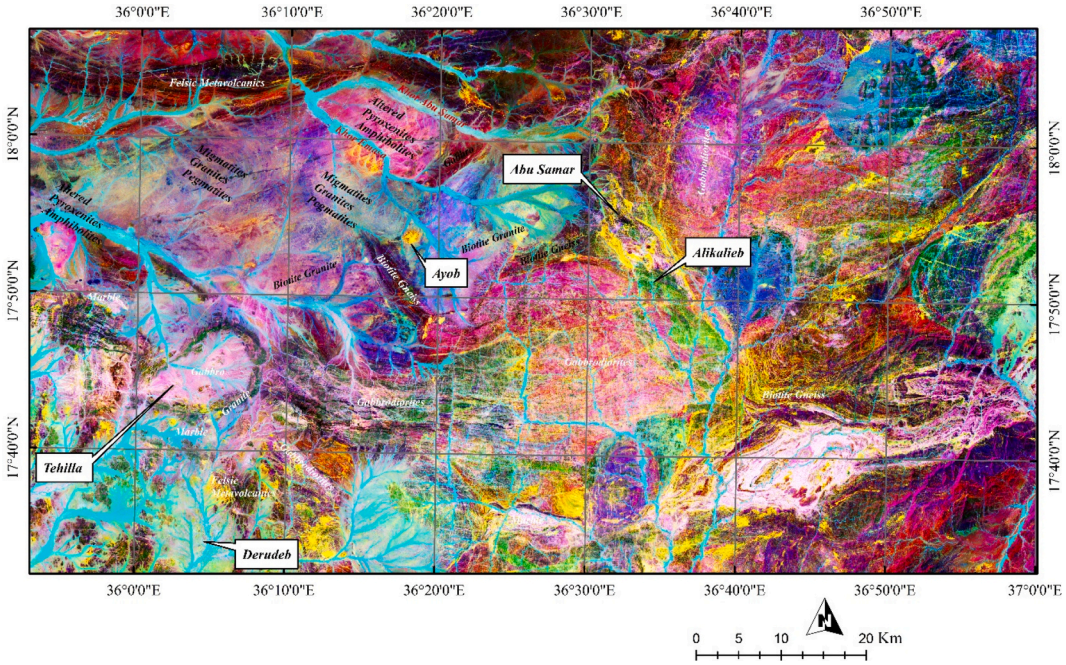


Fig. 6. Composite band image (L9) highlights barite-associated spectral responses and host-rock patterns in yellow, light purple for gabbro, green for metasediments and dark brown for felsic metavolcanics. (For interpretation of the references to colour in this figure legend, the reader is referred to the web version of this article.)

score. Classifier discrimination was further assessed using the area under the receiver operating characteristic curve (ROC–AUC), which summarizes the trade-off between true- and false-positive rates across classification thresholds (Fawcett, 2006). For multiclass classification, ROC–AUC was calculated using a one-vs-rest approach, with macro averaging giving equal weight to all lithological classes and weighted averaging accounting for class sample sizes (Hand and Till, 2001). Statistical differences among classifiers were examined using McNemar's chi-square test (McNemar, 1947) using the stats package in R. Detailed confusion matrices and accuracy statistics are provided in the Appendix, and the overall analytical workflow is summarized in Fig. 2.

3.4. Field and petrographic verification

Field investigations were conducted across the study area to verify the principal lithological and structural features identified from remote-sensing and geophysical interpretation. Representative outcrops of the major mapped lithological units were examined and documented with respect to lithology, texture, weathering characteristics, structural features, and field relationships. Fresh representative rock samples were collected from the principal units for petrographic examination. Standard thin sections were prepared and studied under a polarizing petrographic microscope to identify the dominant mineral assemblages, alteration products, and diagnostic textures. Petrographic observations were used as independent ground-control information to support and refine the lithological interpretation and to assess the consistency of the remotely classified units with field-based geological evidence.

4. Results

4.1. Multisensor spectral enhancement and lithological discrimination

FCCs derived from L8/9 (R7–G5–B3) enhanced regional contrasts among ferruginous surfaces, weathered rocks, and fresh exposures, enabling mapping of major lithological domains such as granitoids, gabbroic bodies, metavolcanic–metasedimentary sequences, greenschist facies, and unconsolidated deposits (Figs. 3a-b). Complementary FCCs from S2 (R12–G2–B1) and ASTER (R5–G2–B1) improved visualization of exposed bedrock and contact zones (Figs. 3a-b). These image products were assessed together with the gravity-derived TAHG output, which highlights linear gradients and boundary-related features (Fig. 3c). Dimensionality-reduction outputs (PCA, ICA, and MNF) enhanced subtle spectral contrasts across the region. PCA composites (e.g., PC7–PC5–PC3) improved separation between gabbroic bodies and adjacent units and emphasized wadi deposits relative to surrounding exposures (Fig. 4a). S2 PCA composites further enhanced discrimination between gabbroic bodies and granitoid units (Fig. 4b).

Targeted band-ratio composites (6/7–5/4, 5/6, 4/2 in RGB respectively) produced coherent spatial patterns that distinguish metavolcanics, granitoids, gabbroic bodies, and high-response zones captured by alteration-sensitive ratios (Fig. 4c). Barite-sensitive indices listed in Table 3 generated localized high-response zones expressed in multisensor outputs (Fig. 4d). Additional composite schemes emphasized ferric-rich zones and associated halos expressed as distinct responses in RGB products (Figs. 4e-f). ASTER-based MNF, PCA, and BR outputs provided additional separability among granitoids, metavolcanics, and weathering products (Figs. 5a–c). Optimized band-ratio combinations highlighted barite-sensitive zones in yellow colour and associated host-rock patterns at the regional scale, including high-response areas extending beyond the primary study boundary (Fig. 6).

Single-ratio products were also generated to emphasize mineral-sensitive responses and alteration patterns, including ferric iron, laterites, ferrous iron, gossan-sensitive responses, barite-sensitive responses, and silica-rich responses across L8/9, S2, and ASTER datasets (Figs. 7–9). These outputs were displayed as grayscale and pseudo-colour images to support consistent interpretation of spectral contrasts in structurally complex terrain. Bands 4/3 (ferric iron), B4/B5 (laterite), B6/B4 and B11/B4 (ferrous iron and gossan), and 6/7–5/4 (barite), and silica (B12/B11) (Figs. 7a-f respectively) across L9, S2, and ASTER datasets proving highly effective delineation of the major alteration zones across the study area.

To improve mineral and alteration-zone detection across the study area, targeted band ratios were applied using sensors selected for their sensitivity to specific mineralogical features associated with ferric and ferrous iron, as well as silicate alteration. The B11/B4 ratio highlights ferrous iron (Fe^{2+}) by capturing near-infrared absorption and

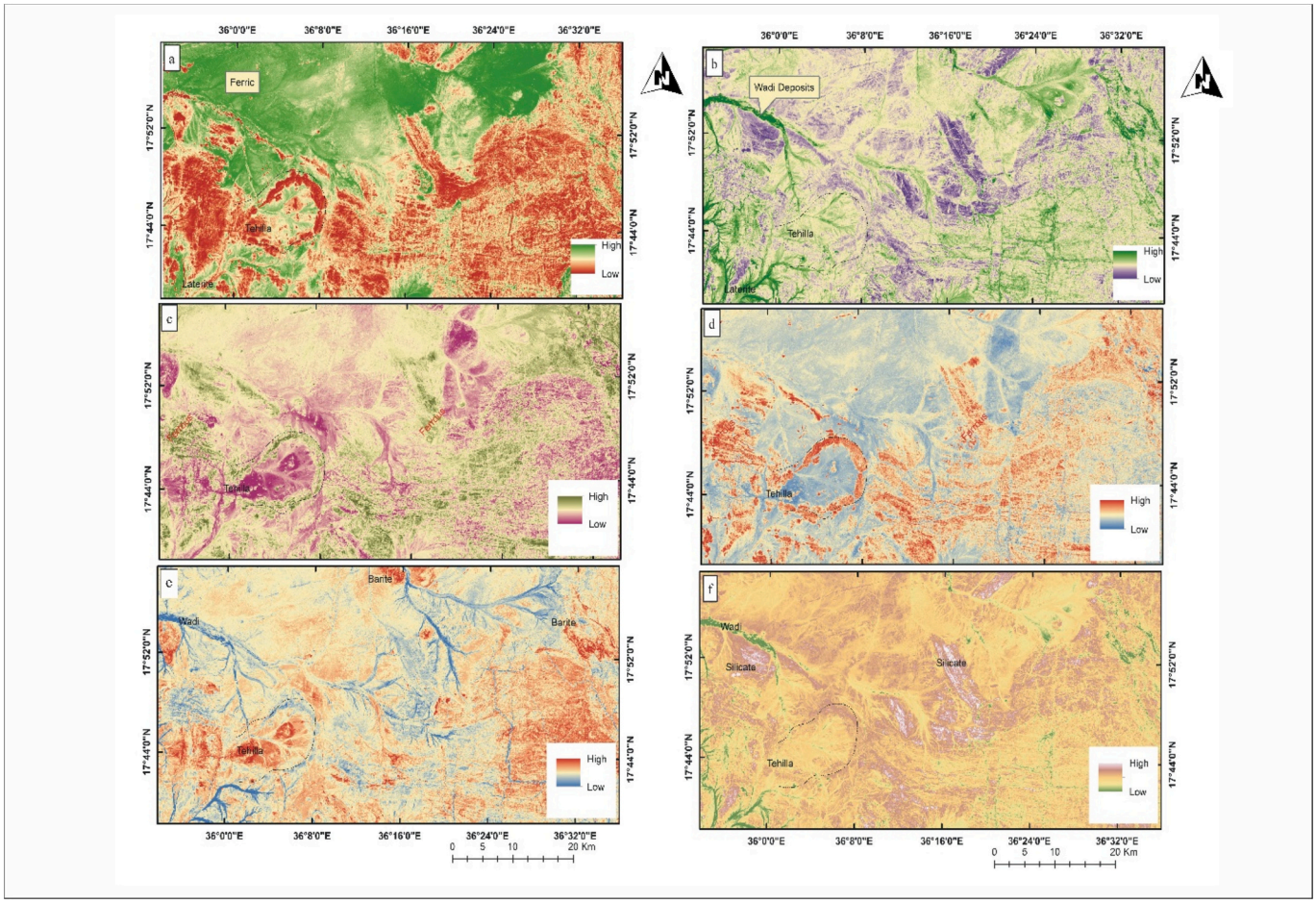


Fig. 7. Sensor-specific band-ratio images highlighting mineral- and alteration-sensitive spectral responses: (a) L8/9 B4/B3, enhancing ferric-oxide responses in green; (b) L9 B4/B5, highlighting lateritic/weathering-related surfaces in green; (c) L8/9 B6/B4, enhancing ferrous-related responses associated with gabbroic rocks; (d) S2 B11/B4, highlighting gossan-related spectral responses; (e) L9 (B6/B7) − (B5/B4), highlighting barite-associated spectral responses in dark red; and (f) S2 B12/B11, enhancing silica- and lithology-sensitive responses in white. (For interpretation of the references to colour in this figure legend, the reader is referred to the web version of this article.)

shortwave-infrared reflectance, often indicating minerals, such as biotite, pyroxene, or chlorite (Fig. 8a). The B13/B14 typically derived from ASTER's thermal infrared bands helps distinguish altered and unaltered silicate-rich rocks, thus identifying hydrothermal alteration zones (Fig. 8b). The B4/B2 ratio reveals total iron oxides; therefore, it is useful for mapping laterites and oxidized zones (Fig. 8c). The B6/B8A ratio detects Fe^{3+} and clay minerals, highlighting hydrothermal halos and secondary alteration minerals (Fig. 8d). The B12/B13 ratio is sensitive to variations in SWIR absorption features, thereby distinguishing felsic rocks altered by hydrothermal processes and enriched in minerals such as kaolinite or alunite (Fig. 8e). Lastly, the B5/B4 ratio targets ferrous silicate minerals, such as chlorite and amphibole, providing key insights into mafic compositions and greenschist-alteration facies, as well as some wadi and Quaternary deposits (yellow colour) (Fig. 8f).

Due to ASTER's high sensitivity in VNIR bands, the ratio of B2/B1 (Fig. 9a) is commonly used as a standard for enhancing ferrous iron-bearing minerals. The band B4/B7 (Fig. 9b) highlights Al-OH absorption features, aiding in the identification of clay minerals, such as kaolinite and montmorillonite. B4/B5 (Fig. 9c) is used for iron oxide detection, particularly hematite and goethite, exploiting their distinct absorption in SWIR bands. B14/B13 (Fig. 9e) targets quartz and siliceous rocks by leveraging the spectral contrast in the TIR region. Finally, bands 6 and 8 are indicators of carbonate minerals (e.g., calcite and dolomite), effectively identifying marbles and their weathered products used for structural dissections (Fig. 9d). In contrast, band B/B4 (Fig. 9f) is sensitive to Ba-Fe-bearing silicates, such as barite, in our study area. These standard ratios, derived from the spectral properties of different sensors L9, L8, S2, and ASTER bands, were complemented by PCA, MNF, and FCC to improve lithological discrimination in selected areas and near the border (see Figs. 10a-f).

4.2. *PRISMA hyperspectral results*

PRISMA hyperspectral imagery provided detailed spectral characterization of the TRC across approximately 240 VNIR–SWIR bands. The imagery was pan-sharpened to a 5 m output grid to improve visualization of lithological boundaries and internal spatial variability. The MNF4–MNF5–MNF6 RGB composite enhanced contrasts among the principal lithological units within and around the TRC, including granitoids, gabbroic rocks, marble, greenschist, and metavolcano-sedimentary assemblages (Fig. 11a). SMACC-derived spectral information further delineated granitoid domains within the study area (Fig. 11b), whereas the pseudocolor representation of MNF4 emphasized the distribution and internal variability of gabbroic rocks within the ring complex (Fig. 11c).

The SMACC abundance products displayed additional spatial variations among the principal lithological and mineral-related spectral responses. Endmember 10 differentiated the post-orogenic younger granite forming the ring complex from granitoid rocks occurring outside the TRC (Fig. 11d). The abundance maps of Endmembers 6, 11, and 12

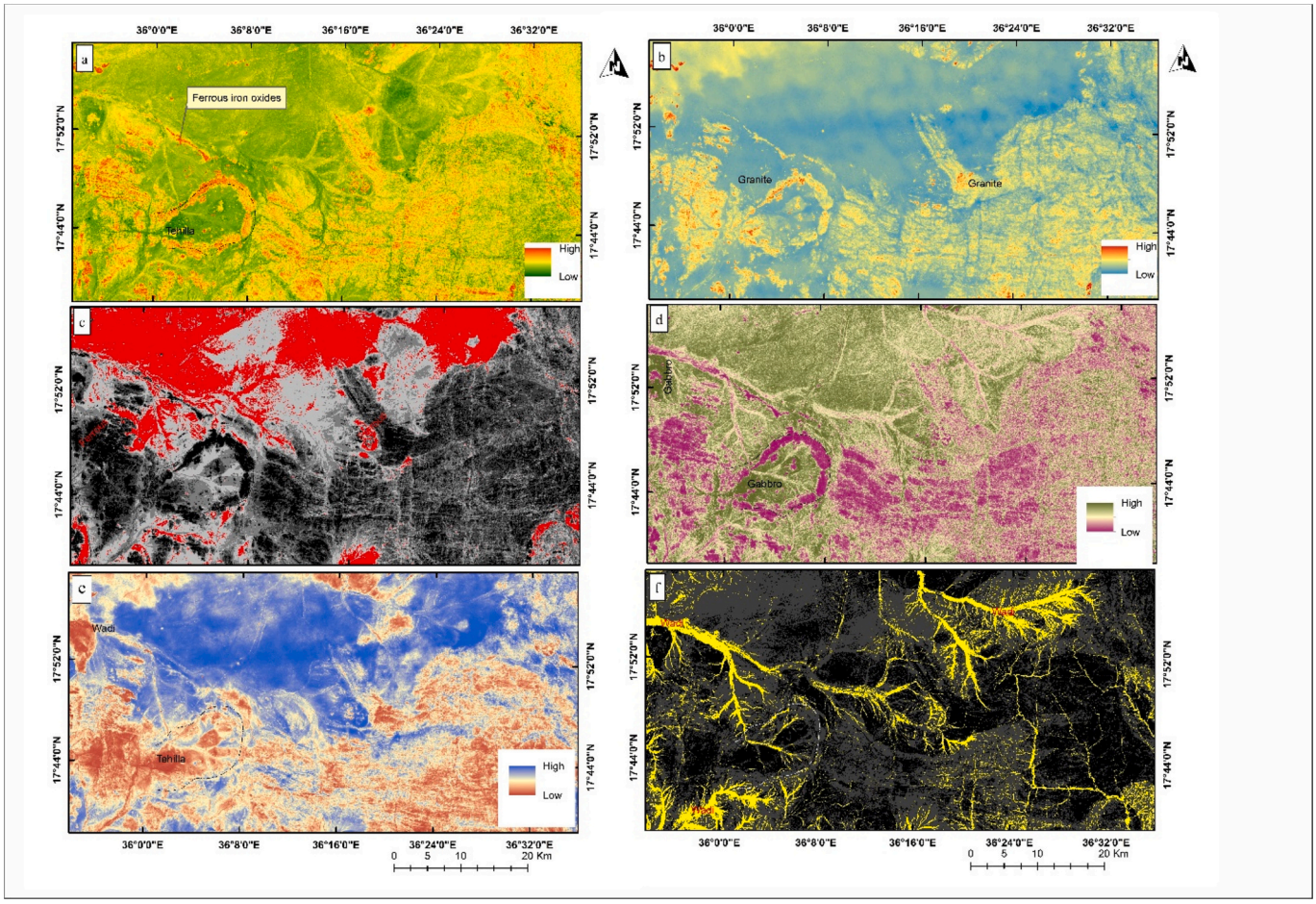


Fig. 8. Sensor-specific band-ratio images highlighting mineral- and alteration-sensitive spectral responses within and around the TRC: (a) S2 B11/B4, enhancing ferrous−/alteration-related spectral responses within the ring complex; (b) ASTER B13/B14, emphasizing silicate-related spectral variations; (c) L8/9 B4/B2, highlighting iron-oxide-rich surfaces; (d) S2 B6/B8A, enhancing Fe- and alteration-related responses; (e) ASTER B12/B13, emphasizing spectral variations associated with biotite-, apatite-, and amphibole-bearing rocks in the central and western parts of the ring complex; and (f) ASTER B5/B4, highlighting ferrous-silicate/lithological variations.

showed contrasting spatial distributions associated with the metavolcano-sedimentary succession and carbonate- and sulfate-sensitive spectral responses, including concentrations in the southern part of the TRC and along structurally disrupted zones (Figs. 11e–g). In addition, the PRISMA 190–187–140 RGB composite enhanced spectral responses spatially associated with documented barite occurrences around the ring complex (Fig. 11h). These responses were subsequently evaluated together with mapped lithology, field observations, and structural information rather than being treated as uniquely diagnostic of barite mineralization.

Spectral profiles of key endmembers were extracted to visualize separability among lithologies (Fig. 12a). Endmember spectra representing granitoid units exhibited similar curve shapes, while endmembers interpreted as marble/barite-related signatures showed distinct differences but also partial overlap (Fig. 12b). Endmember 10 (ring granite) was compared with quartz and muscovite reference spectra, consistent with the felsic composition reported for the complex (Fig. 12c). Endmember 11 was compared with reference spectra of barite and calcite, showing similarity in VNIR and key absorption regions (Fig. 12). Mineralization types associated with barite-hosting lithologies derived from multisensor and PRISMA outputs supported by detailed field observations (Table 6).

4.3. Gravity anomaly results and structural framework

The complete BA map shows regional gravity variations controlled by deep crustal features, with gravity highs over dense mafic rocks, particularly the gabbroic units of the TRC, and lows associated with lower-density rocks and Quaternary sediments (Fig. 13a). The Residual Anomaly map, generated using a 10 km high-pass filter, highlights intrusive contacts and fault-bounded blocks (Fig. 13b). The SVD map enhances lithological boundaries, fault systems, shear zones, and density transitions linked to hydrothermal activity (Fig. 13c), whereas the TAHG map delineates faults and structural boundaries, revealing dominant NE–SW and NW–SE lineaments interpreted as inherited basement structures and shear zones controlling mineralization (Fig. 13d). Gravity anomalies also correlate with field observations, including folded gneissic units and gabbroic bodies characterized by joint systems and spheroidal weathering (See Appendix A).

To investigate subsurface geometry, two gravity profiles (A–B and C—D) were constructed across the TRC (Fig. 14). Profile A–B, oriented NE–SW across the NNE–SSW shear zone, reveals a prominent positive gravity anomaly (~20 mGal) centered on the troctolitic gabbro and bordered by minor gravity lows associated with granitic intrusions (Fig. 14a). Modeling indicates that the gabbro is the dominant subsurface unit, extending laterally beyond its surface exposure and reaching depths of approximately 5 km (Sadig and Ahmed, 1989). Granitic bodies exhibit only minor gravity responses due to their limited subsurface

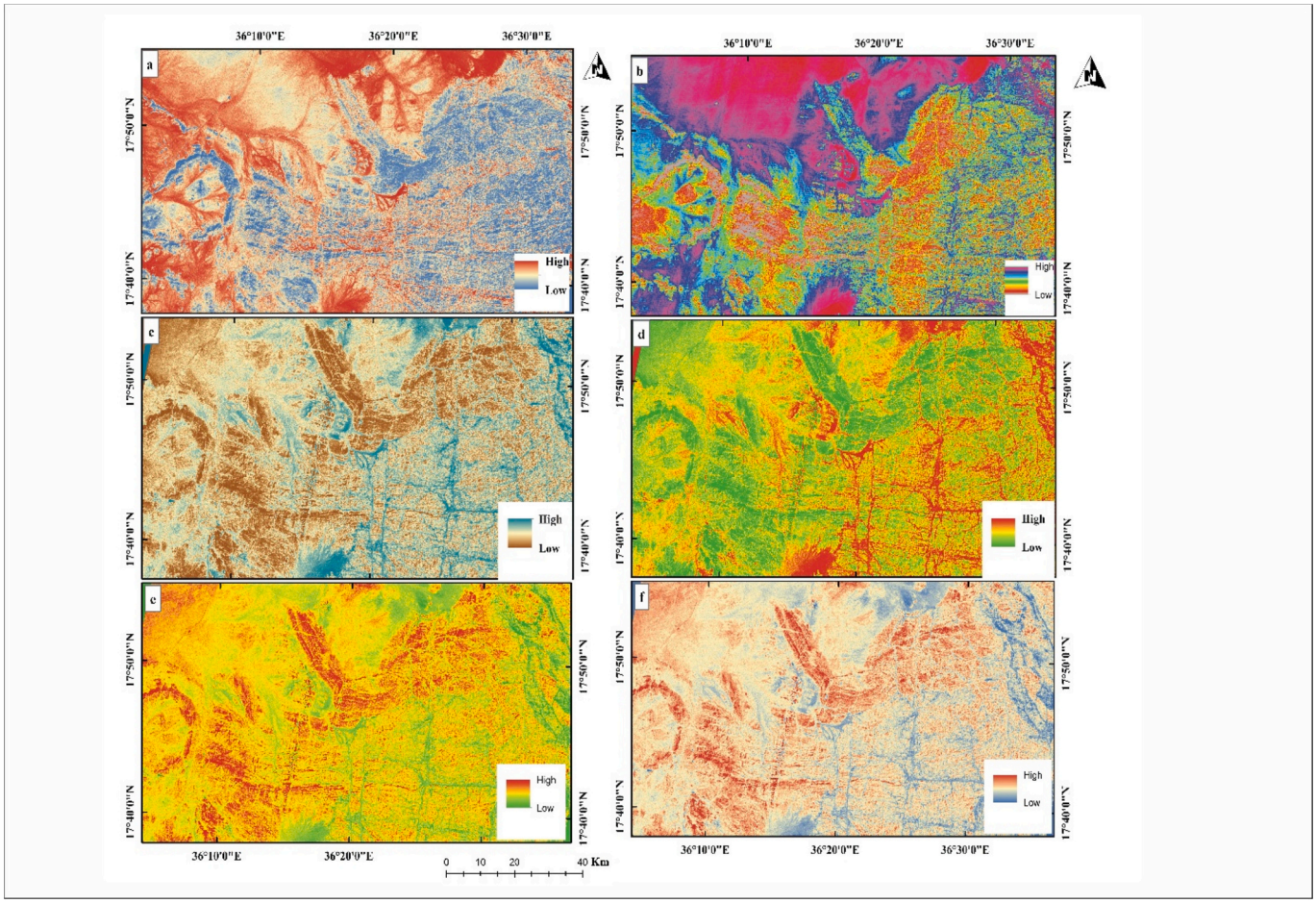


Fig. 9. ASTER band ratio images enhancing specific mineral signatures: (a) ferrous iron (B2/B1) in red, (b) clay minerals (B4/B7) appear in light purple to dark blue, (c) iron oxides (B4/B5), (d) carbonates in green (B6/B8) with clear structure dissections (e) quartz-rich rocks (B14/B13), and (f) Ba—Fe silicates (B5/B4). (For interpretation of the references to colour in this figure legend, the reader is referred to the web version of this article.)

extent (Fig. 14b).

Structural lineaments extracted from gravity-based enhancement techniques (SVD, HG, and TAHG) consistently display dominant NE–SW and NW–SE orientations. Rose diagrams (Fig. 15) summarize these trends and demonstrate that the principal structural directions correspond to major shear zones and fault systems controlling the tectonic evolution of the area. Greater orientation dispersion in the TAHG and integrated datasets reflects the sensitivity of angle-based filters to secondary fractures.

4.4. Data-driven lithological classification results

The five supervised classifiers produced complete lithological classification maps for the ten mapped units across the Tehilla–Abu Samar area (Fig. 16). The final maps generated by XGB, SVM, KNN, RF, and ANN are presented in Figs. 16a–e, respectively, allowing direct comparison of the spatial distribution and boundaries assigned to the lithological classes by each classifier.

The comparative performance of the five supervised classifiers is presented in Table 7 and Fig. 17. XGB achieved an OA of 81.49% with $\kappa = 0.7918$, closely followed by SVM with 81.40% and $\kappa = 0.7908$. KNN and RF produced comparable accuracies of approximately 81%, whereas ANN achieved 75.85%. Macro-F1 values showed a similarly narrow range among XGB, SVM, KNN, and RF.

Class-level performance is presented by the normalized confusion matrices in Fig. 17 and by the PA, UA, and F1 comparisons in Fig. 18, with the complete numerical values provided in Appendix C. For SVM, Quaternary deposits recorded 100% PA and 100% UA, while wadi deposits recorded 99.15% PA and 99.57% UA. The lowest SVM producer accuracy was obtained for *syn-* to late-tectonic granite (53.75%), whereas rhyolite recorded a UA of 70.27%. The confusion matrices document the distribution of correct and incorrect predictions among all ten classes without assigning geological causes to these patterns in the present section (Figs. 17 and 18).

RF, XGB, and KNN showed strong multiclass discrimination, with macro ROC-AUC values of 0.979, 0.978, and 0.956, respectively. Macro PR-AUC values were 0.845, 0.841, and 0.837, indicating similarly strong but more conservative precision–recall performance. The strongest discrimination occurred for Quaternary and Wadi classes, whereas Syn to Late Granite remained the most challenging lithological unit (see Appendix C).

The spatial extent of the lithological classes derived from the final RF, XGB, and KNN maps is summarized in Table 8. Wadi deposits occupied 19.06–23.54% of the mapped area, followed by Quaternary deposits at 14.81–17.40%. Granodiorite, gabbro, greenschist, and felsic metavolcanics showed relatively similar mapped proportions among the three classifiers, while greater differences were observed for metasediments, Syn- to Late granite, and rhyolite. The final integrated lithological–structural interpretation incorporating the classification outputs, field observations, spectral products, and gravity-derived structural information is presented in Fig. 19.

Pairwise McNemar testing further distinguished the classifier performances. SVM and ANN showed a highly significant difference in their paired classification outcomes (Table 9). In contrast, none of the

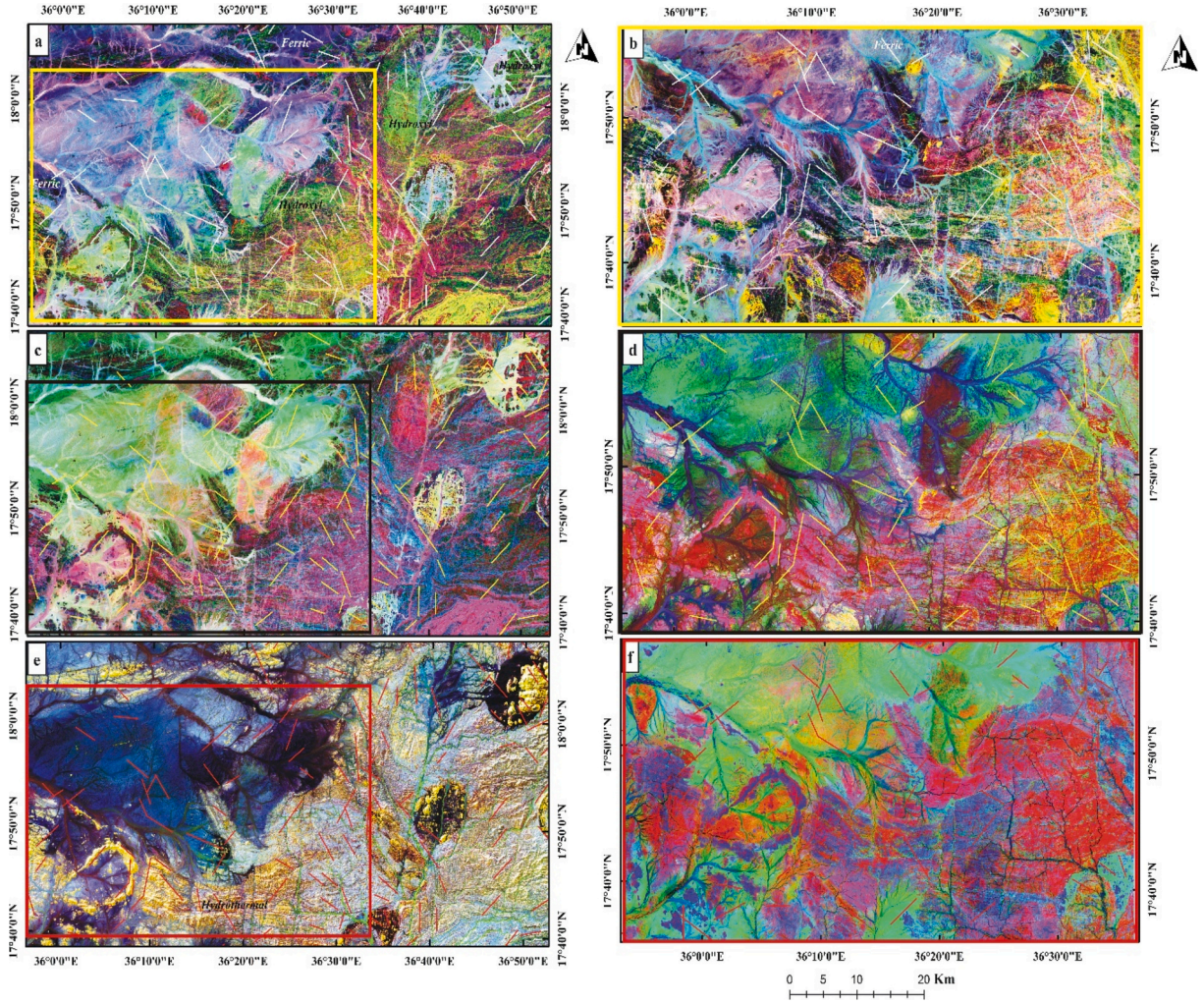


Fig. 10. Lithological discrimination of different multisensor data (a) L9 4/2–5/6–6/7 in RGB; (b) PC of 4/2–5/6–6/7, (c) Abram composite band in L8, (d) PC of Abram delineating granitic rocks in light red and dark colour for mafic rocks, (e) ASTER SWIR and TIR bands show silica rich rocks in light yellow, (f) S2 6/4–4/3–4/5 in RGB, respectively. The plotted squares indicate the primary study area along with additional regions involved to enhance mineralogical discrimination and lines for lineaments. (For interpretation of the references to colour in this figure legend, the reader is referred to the web version of this article.)

pairwise comparisons among RF, XGB, and KNN remained statistically significant after Holm correction (padj = 0.0646–0.8411). These results complement the overall accuracy statistics by showing a clear statistical separation between SVM and ANN, whereas RF, XGB, and KNN exhibited statistically comparable prediction outcomes.

Class-wise performance across the five classifiers is summarized in Fig. 18. The PA–UA distributions show broadly similar class-level patterns among SVM, RF, XGB, and KNN, whereas ANN shows greater dispersion for several lithological units (Fig. 18a). The F1-score heatmap further shows that Quaternary deposits attained an F1-score of 1.00 for all five classifiers, while wadi deposits ranged from 0.98 to 1.00 (Fig. 18b). Granodiorite yielded F1-scores of 0.74–0.83, greenschist 0.70–0.80, felsic metavolcanics 0.70–0.79, gabbro 0.72–0.75, metasediments 0.70–0.74, and younger granite 0.72–0.80. Syn- to late-tectonic granite showed F1-scores of 0.56–0.61 for SVM, RF, XGB, and KNN, but 0.12 for ANN. Rhyolite ranged from 0.76 to 0.80 for SVM, RF, XGB, and KNN, compared with 0.42 for ANN. The corresponding PA and F1 distributions for individual lithological units are compared in Fig. 18c, while the complete class-wise statistics are provided in Appendix C.

4.5. Field and petrographic verification

Field investigations and petrographic observations were used to verify the principal lithological and structural features mapped from the remote-sensing and gravity datasets. The field survey documented the main lithological units exposed across the Tehilla–Abu Samar area and provided direct observations of their mineralogical, textural, weathering, and structural characteristics (Figs. 20a–i).

Altered metavolcanic rocks commonly form prominent high-relief ridges (Fig. 20a), whereas granitic and granitoid bodies occur widely throughout the study area (Fig. 20b, d, e). The granitoids locally contain xenoliths (Fig. 20d) and display pronounced weathering features, including onion-like weathering and exfoliation (Fig. 20g–i). Gabbroic rocks are generally massive to weakly foliated and locally weather into spheroidal boulders (Fig. 20c). Granodiorite was also identified in the field as a distinct intrusive unit (Fig. 20f).

The metasedimentary succession is represented principally by marble, which is locally fractured and affected by structures associated with the Tehilla shear zone. Intrusive rocks of the TRC are dominated by alkaline granitic rocks with pronounced jointing, accompanied by gabbroic rocks within the central part of the complex. Quaternary deposits and unconsolidated wadi sediments occupy drainage channels, valleys, and other low-lying areas.

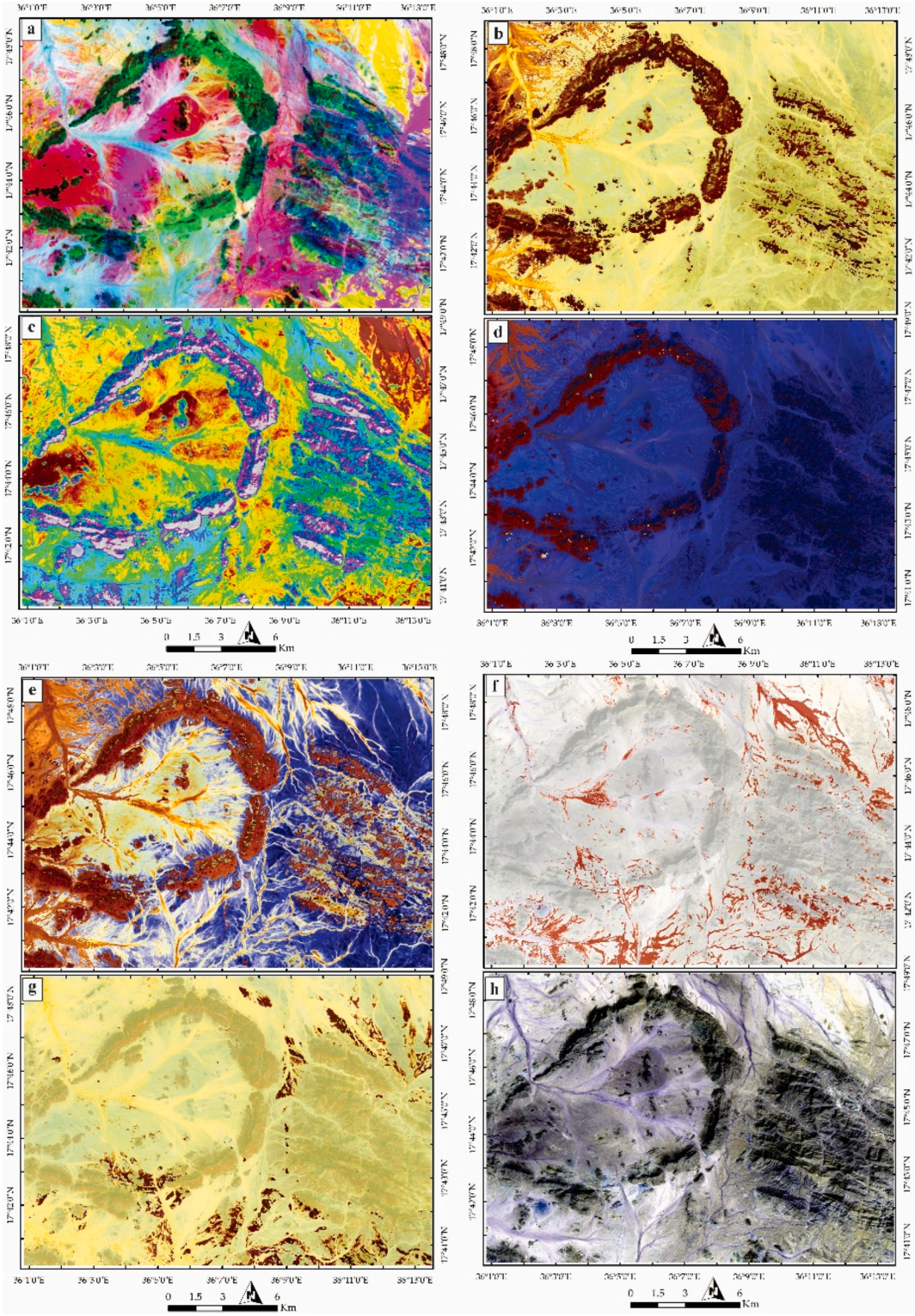


Fig. 11. PRISMA based lithological discrimination of (a) MNF of bands 4–5-6 highlights major lithological units; (b) SMACC delineating granitoids in brown; (c) Pseudocolor ramp of MNF4 highlights gabbro in brown; (d) Abundance map of Endmember 10 differentiates the post-orogenic younger granites (ring complex); (e) The abundance map of Endmember 6, (f) Endmember 11, (g) Endmember 12, (h) FCC of bands 190–187–140 in RGB delineating barite-bearing locations in blue around the ring complex. (For interpretation of the references to colour in this figure legend, the reader is referred to the web version of this article.)

Field structural observations documented foliation, joints, fractures, and shear-related fabrics corresponding spatially with the principal structural features mapped from satellite imagery and gravity-derived products (see Appendix).

Petrographic examination of representative samples further confirmed the principal lithological assignments. Granodiorite is characterized by plagioclase, quartz, hornblende, and biotite, whereas gabbro contains plagioclase, pyroxene, hornblende, and subordinate biotite and olivine. Metavolcanic rocks include meta-andesite, metabasalt, and meta-rhyolite, with assemblages dominated by plagioclase, quartz,

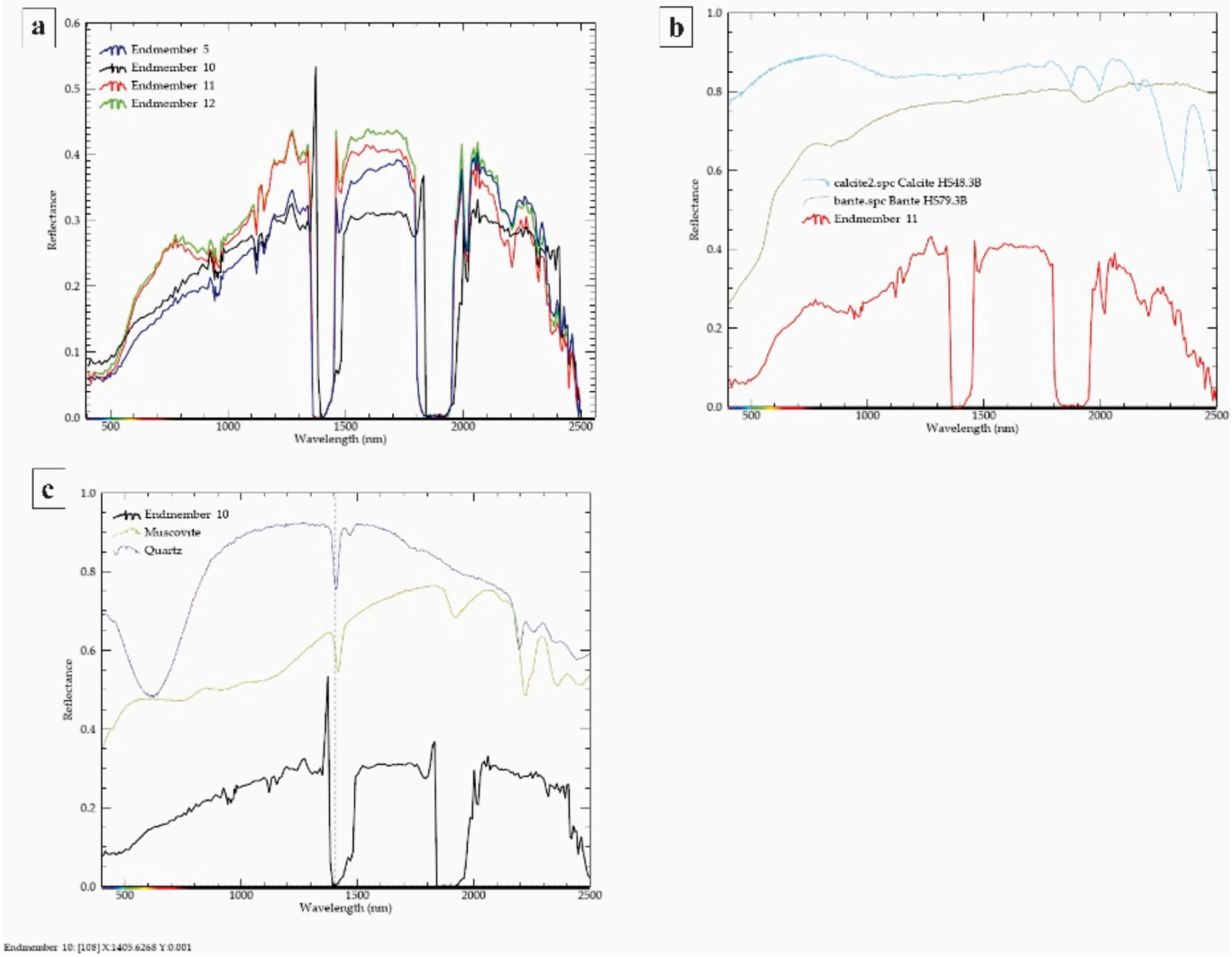


Fig. 12. (a) VNIR–SWIR spectra of the principal extracted endmembers; (b) abundance map of Endmember 11, interpreted as a mixed barite–calcite spectral response; and (c) Endmember 10 spectrum, interpreted as a quartz–muscovite-rich felsic assemblage based on comparison with the USGS Spectral Library and geological constraints.

Table 6
Mineral occurrences associated with barite and host lithologies in the Tehilla–Abu Samar area.

Mineral/occurrence	Resource potential	Location in map (Fig. 1b and Fig. 19)
Barite	Principal ore mineral of barium	SW of Tehilla and Abu Samar
Quartz	Hydrothermal activity and alteration zones	
Marble	–	Derudeb, Tehilla
Tin	Derived from pegmatite	Within granitoids
Copper	Metavolcanics, barite veins	Derudeb, Abu Samar
Vermiculite	Hydrothermal alteration of gneisses	
Manganese	Associated with barite veins	Abu Samar
Lead	Associated with barite veins	
Tungsten	Granitic rocks	
Iron titano-magnetite	Gabbroic rocks	Tehilla
Kaolin	Alteration of acidic volcanic rocks	Derudeb
Gossan and massive sulfide	Massive pyrite as primary mineralization	
Tourmaline	Boron-rich hydrothermal alteration	

pyroxene and/or amphibole, accompanied by variable chloritization, sericitization, and metamorphic recrystallization. Marble is composed predominantly of recrystallized calcite, while *syn*-tectonic granite consists mainly of quartz and plagioclase with evidence of strain, recrystallization, and feldspar alteration. These mineralogical and textural characteristics provide independent ground control supporting the lithological discrimination derived from the satellite-based classification. Detailed petrographic descriptions and representative photomicrographs are provided in Appendix D.

Available unpublished geochemical analyses from the Geological Research Authority, Sudan further indicate marked compositional variability in barite from the Tehilla–Abu Samar area, with $BaSO_4$ contents ranging from 35.50 to 93.62 wt% and variable enrichment in SiO_2, Fe_2O_3, and MnO. These variations are consistent with heterogeneous barite purity and variable hydrothermal alteration and gangue influence; detailed geochemical data are presented in Appendix D.

5. Discussion

5.1. Spectral characteristics and mineralogical implications

The multispectral and hyperspectral results are consistent with the established geological framework of the Derudeb district, where the TRC

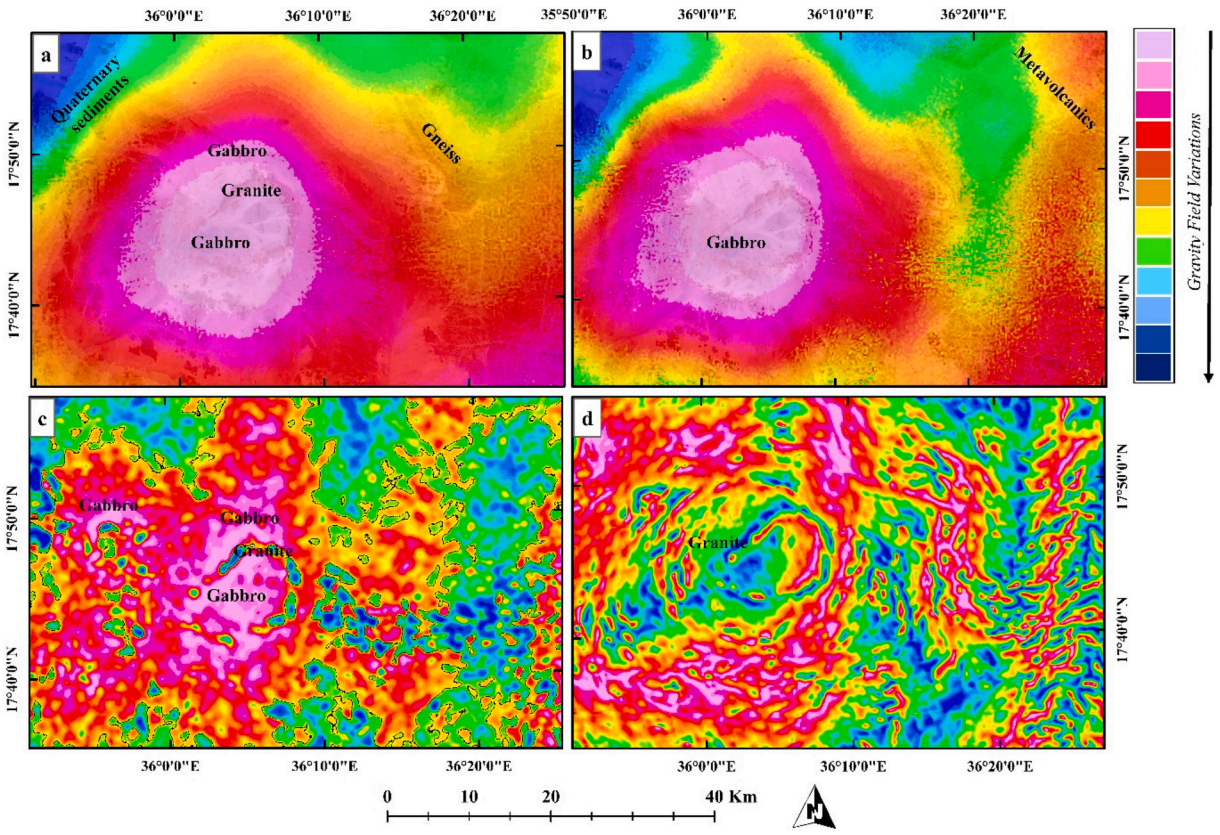


Fig. 13. Gravity maps of (a) Bouguer anomaly, (b) Residual 10 km, (c) SVD, (d) TAHG map.

comprises felsic and mafic intrusive phases surrounded by metavolcanic, metasedimentary, and carbonate-bearing successions (Ahmed, 1977; Elsamani et al., 2001; (Kenea et al., 2001;); Satti et al., 2026). This study extends previous geological investigations by integrating regional multispectral observations, PRISMA hyperspectral data, and field-based geological control, which enables a comprehensive assessment of the principal lithological domains and their spectral variability. The spectral characteristics and spatial distribution of PRISMA Endmember 10 suggest a quartz–muscovite-rich felsic assemblage associated with the granitic components of the TRC, in agreement with previous descriptions of leucocratic and alkaline granitic phases (Abu-Fatima et al., 2021; Adam et al., 2024; Elsamani et al., 2001; (Kenea et al., 2001)). Additional extracted endmembers, concentrated within metavolcanic–metasedimentary and carbonate-bearing domains, display mixed carbonate- and sulfate-sensitive VNIR–SWIR responses. The spatial distribution of these endmembers is relevant for mineral exploration, as documented barite occurrences in the Derudeb district are linked to volcano-sedimentary successions, carbonate-rich units, lithological contacts, and structurally controlled mineralization (Elsamani et al., 2001; Satti et al., 2026).

Field observations provide independent constraints on these interpretations. The field survey verified the presence and spatial relationships of the principal mapped units, including altered metavolcanics, granitoids, gabbro, granodiorite, marble-bearing metasediments, and intrusive rocks of the TRC (see Fig. 20). Petrographic analysis further defined their mineralogical and textural characteristics. Additionally, geochemical analyses of selected barite samples from the Tehilla–Abu Samar area provide compositional support for the sampled occurrences; however, they do not constitute analytical validation of unsampled remotely detected anomalies.

The carbonate–sulfate-sensitive responses detected by ASTER and PRISMA coincide spatially with field-confirmed barite occurrences and barite-bearing samples geochemically characterized within the Tehilla–Abu Samar area. This correspondence provides independent ground support for interpreting these spectral responses in relation to barite-bearing lithologies. Nevertheless, the spectral response itself is not uniquely diagnostic of barite, because sulfate-, carbonate-, and hydroxyl-bearing minerals, alteration products, and weathered surfaces may exhibit overlapping VNIR–SWIR absorption features (Daoud et al., 2025; Elfadly et al., 2026; Hubbard et al., 2024; Shebl et al., 2024). Accordingly, spectral anomalies coincident with the field- and geochemically verified barite occurrences are regarded as validated barite-associated spectral responses, whereas similar anomalies extending beyond the sampled localities are considered prospective barite-associated targets requiring additional field verification.

The complementary characteristics of the optical datasets underscore the advantages of multisensor interpretation. L8/9 and S2 provide regional lithological and surface compositional information; ASTER offers SWIR sensitivity to alteration- and mineral-related spectral variations, and PRISMA supplies finer spectral sampling for detailed mineralogical analysis. Unlike single-sensor approaches, the current workflow enables cross-comparison of responses across independent spectral, lithological, structural, and field datasets (Abdelkareem et al., 2024; Abo Khashaba et al., 2026; Bedini and Chen, 2020). Importantly, these datasets were processed through complementary workflows and integrated during geological interpretation, rather than being merged into a single machine-learning predictor stack.

5.2. *Gravity constraints, structural controls, and tectonic framework*

Gravity analysis provides a subsurface perspective that complements the predominantly surface-sensitive remote-sensing observations. The Bouguer anomaly high centered over the TRC, along with the modeled subsurface geometry, suggests a relatively dense mafic body extending to approximately 5 km depth beneath the complex. This interpretation is consistent with previous geological descriptions of a significant gabbroic

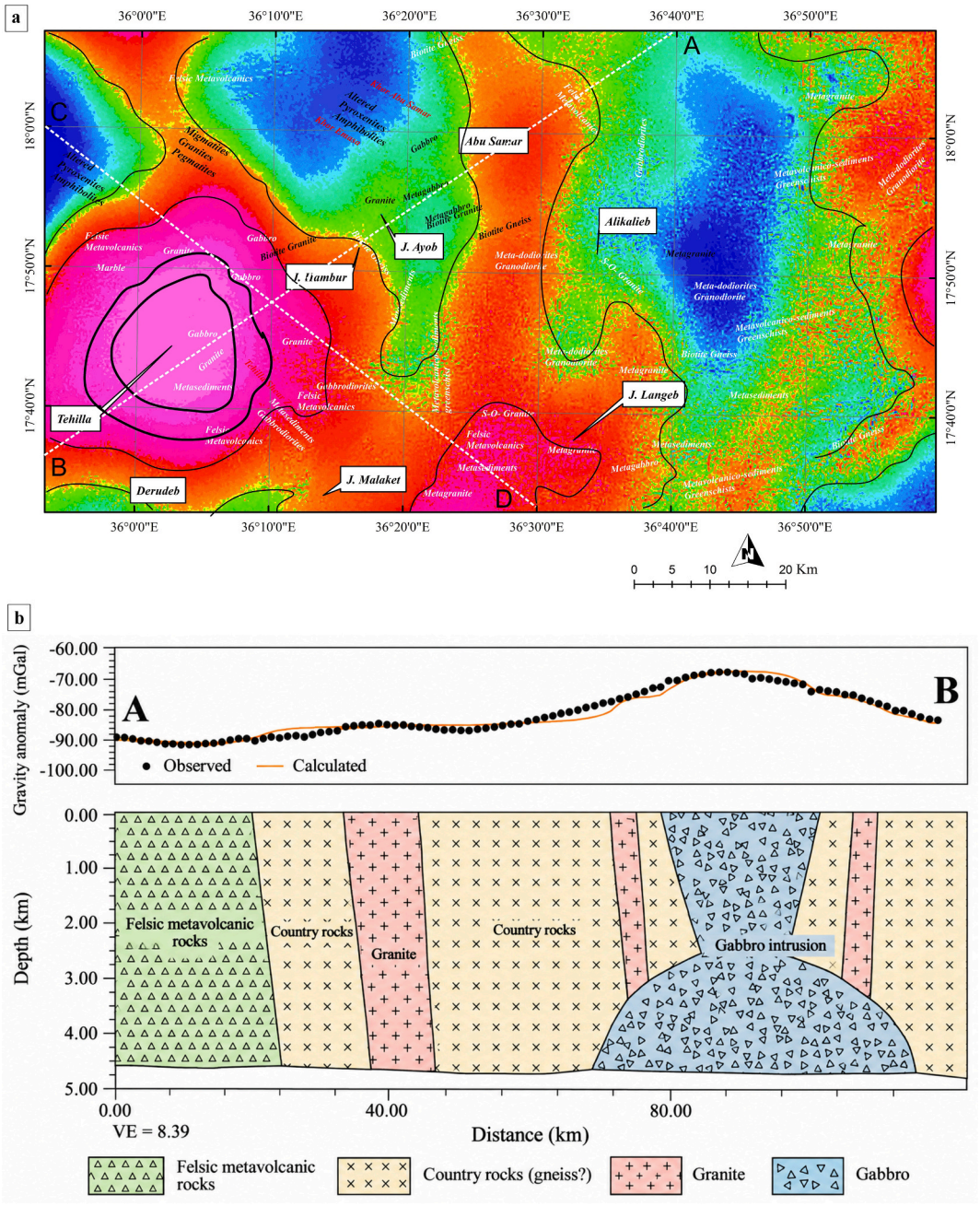


Fig. 14. (a) Gravity profile A-B across the ring complex in the Residual Bouguer anomaly map; (b) Conceptional gravity profile (A-B) along TRC.

component within the TRC and with earlier regional interpretations of mafic intrusive activity in the RSH (Sadig and Ahmed, 1989; Vail, 1985). The inward-dipping geometry derived from the modeling supports a lopolith-like mafic body, while the weaker gravity response of the felsic components indicates a more limited subsurface extent.

Residual gravity, along with the SVD, HG, and TAHG products, accentuates lateral density contrasts associated with intrusive contacts, lithological boundaries, and structural discontinuities. The dominance of NE–SW and NW–SE orientations in the gravity-derived lineaments broadly aligns with major structural trends documented in the RSH and the ANS (Abdel Rahman, 1993; Abdelsalam, 2010; Eldosouky et al., 2022; Stern and Abdelsalam, 1998). The alignment of these lineaments with field-observed shear zones, fractures, foliations, and intrusive boundaries reinforces their interpretation within the regional structural framework.

These observations are consistent with a polyphase deformation history characterized by early folding, progressive shear-zone development, structural reactivation, and subsequent extensional deformation. Previous regional studies have attributed late deformation and dyke emplacement to the reactivation of inherited crustal fabrics during post-orogenic extension and later tectonic reworking (Abdel Rahman, 1993; Abdelsalam, 2010; Shang et al., 2010; Stern and Abdelsalam, 1998). The persistence of NE–SW and NW–SE orientations across multiple independently derived gravity products supports long-lived structural inheritance in the study area. This structural setting is significant for hydrothermal mineralization, as major fractures, shear zones, intrusive contacts, and reactivated structures can serve as pathways for hydrothermal-fluid circulation (Abdelrahman et al., 2023; Abd El-Wahed et al., 2025; Daoud et al., 2025; Hamimi et al., 2023; Mahdi et al., 2022). Documented barite occurrences in the Derudeb district are frequently associated with structurally controlled settings. The spatial relationship between barite-bearing localities, host lithologies,

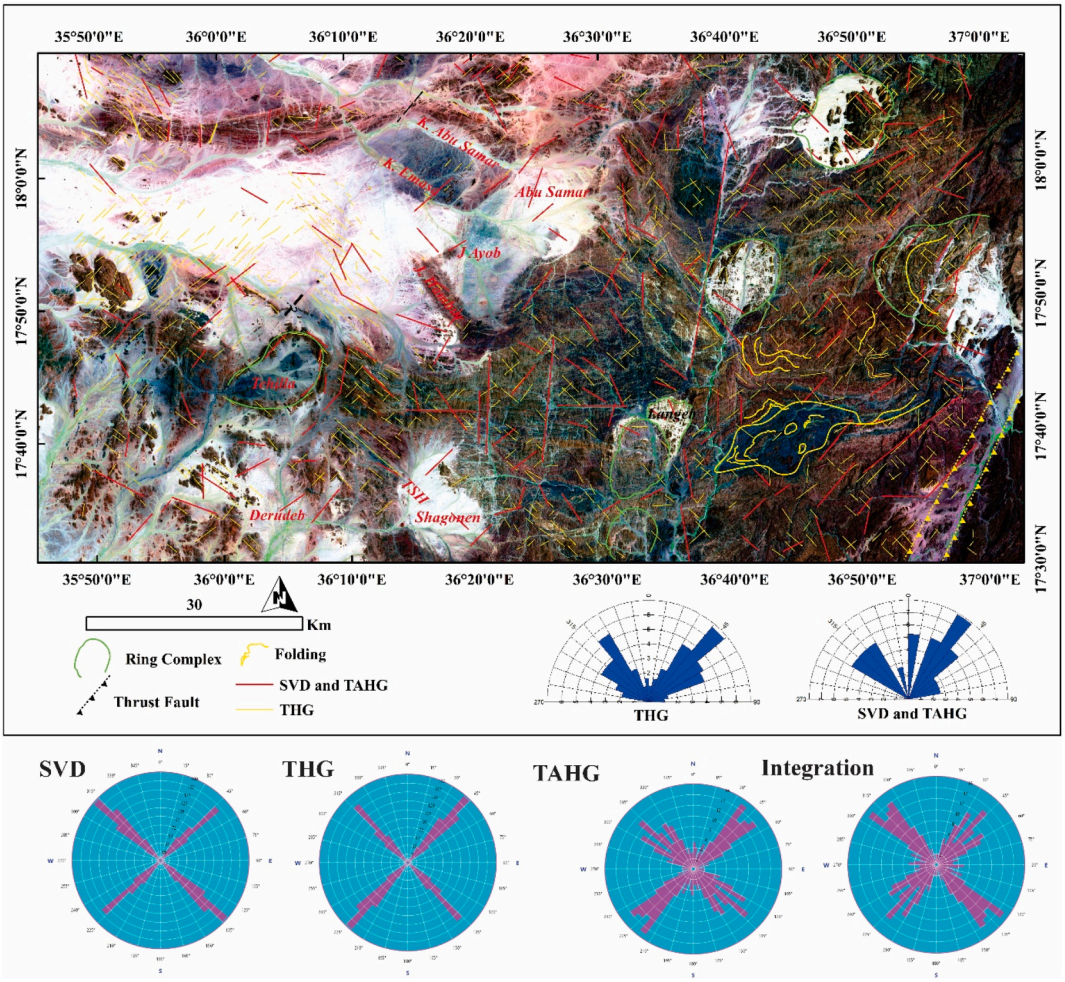


Fig. 15. Structural map of the Derudeb district. Rose diagrams showing the dominant structural orientations interpreted from SVD, THG, TAHG, and integrated gravity-derived lineaments. (For interpretation of the references to colour in this figure legend, the reader is referred to the web version of this article.)

and major structural corridors thus provides a geological rationale for prioritizing exploration targets. However, gravity-derived lineaments represent structural features and do not constitute direct evidence of structurally controlled barite mineralization.

5.3. *Machine-learning performance and lithological discrimination*

The comparison of classifiers reveals closely comparable overall performance among XGB, SVM, KNN, and RF (Table 7). XGB achieved the highest OA and κ, while SVM produced a slightly higher macro-F1 score. KNN and RF yielded similarly close results, whereas ANN exhibited lower classification performance. The narrow performance range among the four leading classifiers indicates that lithological discrimination was primarily influenced by the spectral characteristics and internal variability of the mapped units, rather than by classifier selection alone.

The class-level results corroborate this interpretation (see Figs. 17 and 18; Appendix C), which show that differences among lithological units are more pronounced than the overall differences among the leading classifiers. Quaternary and wadi deposits were consistently identified with high accuracy, while *syn*- to late-tectonic granite and several compositionally related felsic units exhibited greater classification confusion. Statistical comparisons further support the close performance of the principal models: pairwise McNemar tests revealed no significant differences among RF, XGB, and KNN after Holm correction (see Table 9), whereas SVM and ANN demonstrated significant differences in their paired tests.

The limited separability of certain crystalline rock units is geologically reasonable. Granitic, granodioritic, rhyolitic, and felsic metavolcanic rocks often share overlapping quartz–feldspar assemblages and can develop similar surface spectral characteristics, particularly in arid environments (Dadi et al., 2024; Grebby et al., 2016; Johnson et al., 1989). Weathering, oxidation, alteration coatings, grain-size variations, spectral mixing at contacts, and topographic effects can further influence these spectral responses (Younis et al., 1997). Comparable challenges in distinguishing compositionally related granitoid and metavolcanic units have been documented in other remote-sensing lithological studies (Abo Khashaba et al., 2026; Hubbard et al., 2024; Orynbassarova et al., 2025). In contrast, unconsolidated Quaternary and wadi deposits differ from crystalline bedrock in composition, surface texture, geomorphic setting, and spectral behavior.

Mapped-area statistics offer further comparison among the final RF, XGB, and KNN classifications (See Table 8). Gabbro, granodiorite, felsic metavolcanics, and greenschist occupy similar proportions across the three maps, while metasediments, syn- to late-tectonic granite, rhyolite, Quaternary deposits, and wadi sediments display greater variability. These findings indicate that classifiers with comparable overall accuracy may still assign different spatial extents to specific geological units, especially along heterogeneous boundaries and spectrally transitional contacts.

Comparison with previous geological maps of the Haya terrane highlights the value of the updated digital classification (Abu-Fatima

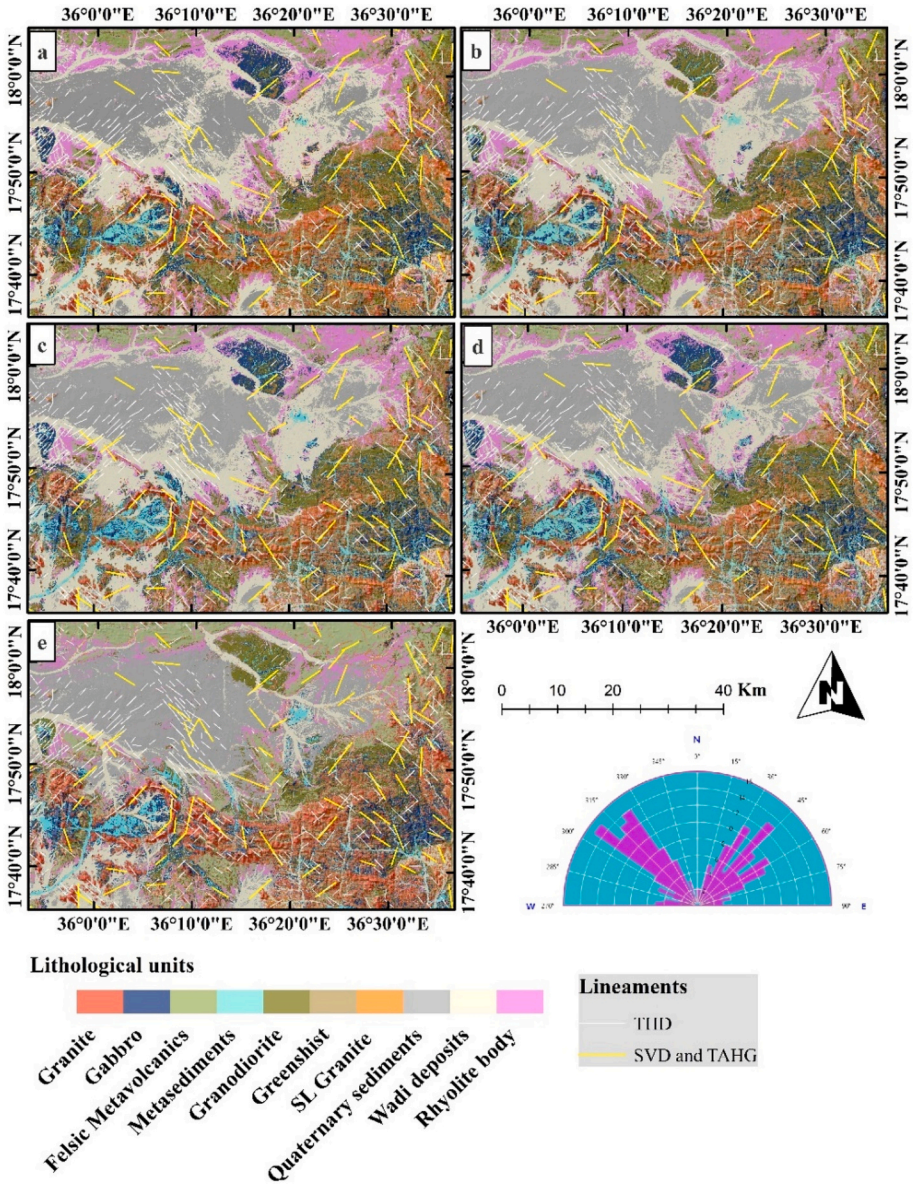


Fig. 16. Lithological classification maps of the Tehilla–Abu Samar area generated using (a) XGB, (b) SVM, (c) KNN, (d) RF, and (e) ANN classifiers, showing the spatial distribution of the mapped lithological classes.

Table 7
Overall performance of the supervised classifiers used for lithological mapping.

Classifier	Overall Accuracy (%)	Kappa (κ)	Macro-F1
XGB	81.49	0.7918	0.7962
SVM	81.40	0.7908	0.7967
KNN	80.82	0.7843	0.7929
RF	80.71	0.7831	0.7908
ANN	75.85	0.7260	0.6836

et al., 2021; Adam et al., 2024; Daoud et al., 2025; Elsamani et al., 2001; (Kenea et al., 2001)). The machine-learning outputs enable spatially continuous discrimination of the principal lithological units and facilitate comparison of intrusive, metavolcanic, metasedimentary, and surficial domains at the satellite imagery scale. However, these classifications remain complementary to field geological mapping, especially where spectrally similar lithologies are present along structurally complex contacts.

5.4. Integrated framework and implications for barite exploration

The principal value of the integrated framework lies in the complementary geological information provided by the different datasets rather than in their fusion into a single predictive model. Multispectral imagery characterizes regional lithological and mineral-sensitive surface variations, whereas PRISMA provides higher spectral dimensionality for evaluating mineralogical differences and diagnostic absorption features. Supervised classification supplies spatially continuous lithological information, field and petrographic observations provide geological control, and gravity-derived products constrain subsurface density contrasts, intrusive architecture, and major structural boundaries. The independent comparison of these datasets reduces reliance on any single source of information and is particularly important in the TRC, where intrusive contacts, metavolcanic–metasedimentary successions, shear zones, and hydrothermal occurrences form a spatially complex geological system. This complementary approach therefore provides a more geologically constrained interpretation than single-sensor analysis, in which spectral ambiguity, spatial resolution, surface conditions, or

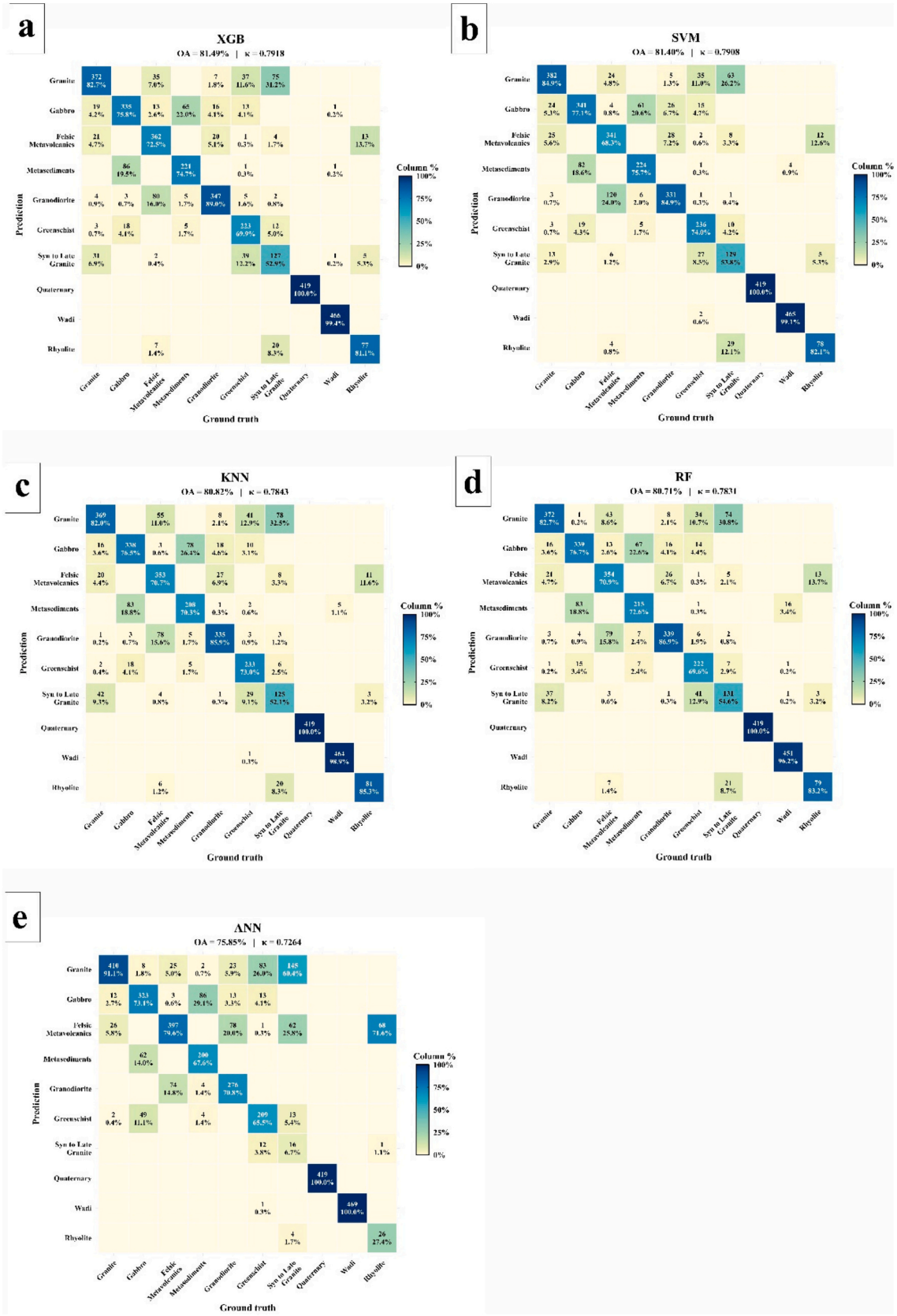


Fig. 17. Normalized confusion matrices for (a) XGB; (b) SVM; (c) KNN; (d) RF; and (e) ANN classifiers, showing predicted versus reference lithological classes for the validation dataset.

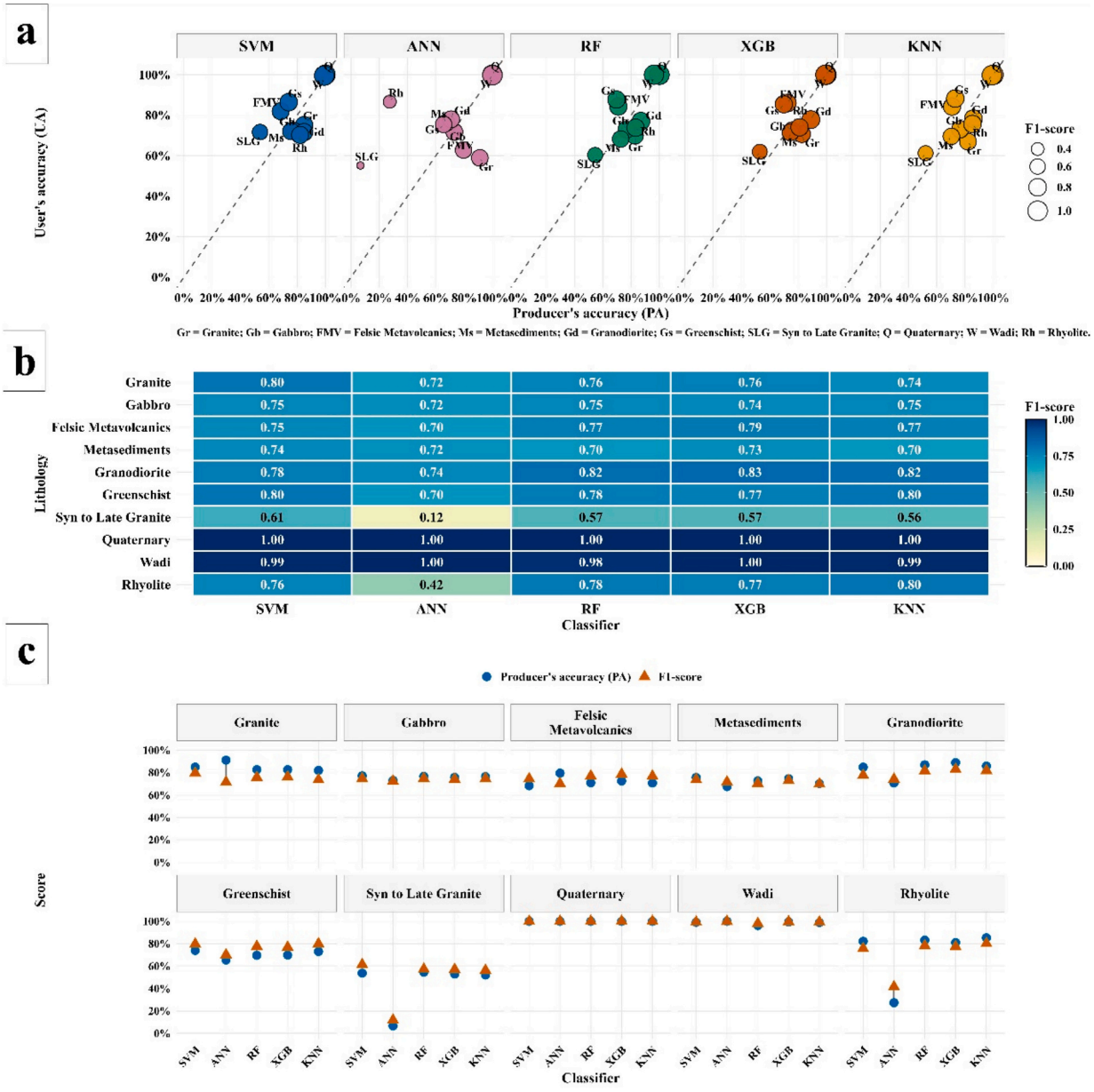


Fig. 18. Class-level performance of the five supervised classifiers for lithological mapping. (a) PA versus UA for each lithological class and classifier, with marker size proportional to the F1-score; (b) class-wise F1-score heatmap for SVM, ANN, RF, XGB, and KNN; and (c) comparison of PA and F1-score among classifiers for each lithological unit.

Table 8
Lithological areas derived from the final RF, XGB, and KNN classification maps.

Lithological unit	RF area (km^2)	RF (%)	XGB area (km^2)	XGB (%)	KNN area (km^2)	KNN (%)
Younger granite	244.22	6.12	249.97	6.27	267.88	6.71
Gabbro	409.71	10.27	385.37	9.66	386.95	9.70
Felsic metavolcanics	268.62	6.73	267.07	6.69	278.58	6.98
Metasediments	210.07	5.27	139.47	3.50	167.98	4.21
Granodiorite	437.76	10.97	460.86	11.55	454.48	11.39
Greenschist	311.99	7.82	297.16	7.45	303.13	7.60
Syn- to late-tectonic granite	176.66	4.43	214.12	5.37	146.53	3.67
Quaternary deposits	694.23	17.40	590.99	14.81	649.24	16.27
Wadi deposits	760.49	19.06	907.02	22.73	939.28	23.54
Rhyolite	475.89	11.93	477.59	11.97	395.59	9.92
Total	**3989.64**	**100.00**	**3989.64**	**100.00**	**3989.64**	**100.00**

geophysical non-uniqueness may dominate the resulting interpretation (Abo Khashaba et al., 2026; Asghede et al., 2025; Satti et al., 2026; Yuan et al., 2026).

Field observations and geochemical analyses establish the felsic

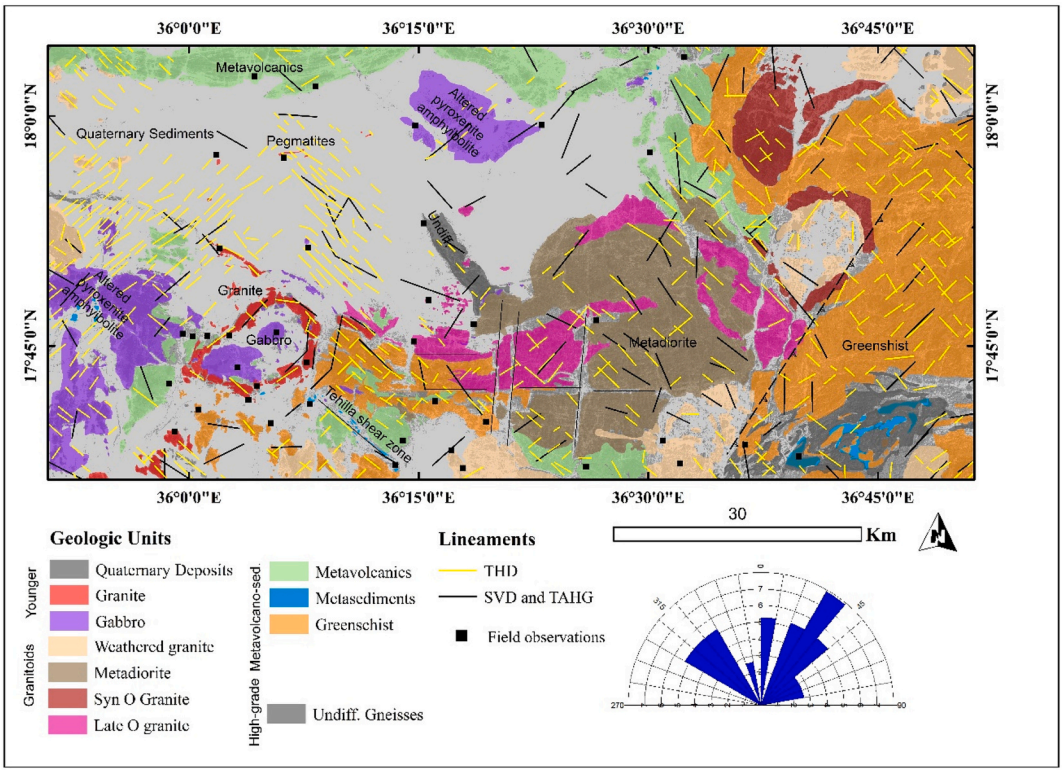


Fig. 19. Integrated lithological map of the Tehilla–Abu Samar area derived from multisensor remote sensing datasets, gravity-derived structural information, and supervised machine-learning algorithms.

Table 9
Pairwise McNemar tests for the supervised lithological classifiers.

Model comparison	χ^2	*p*-value	Holm-adjusted p	Statistical outcome
SVM vs ANN	106.10	$<2.2 \times 10^{-16}$	—*	Significant
RF vs XGB	5.283	0.0215	0.0646	Not significant
RF vs KNN	0.040	0.8411	0.8411	
XGB vs KNN	2.261	0.1327	0.2654	

metavolcanic rocks as the principal host of barite mineralization in the Tehilla–Abu Samar area. This host-rock relationship provides the geological basis for interpreting the remotely sensed sulfate-sensitive responses, particularly where they coincide with mapped felsic metavolcanic units, lithological contacts, and major structural settings (Daoud et al., 2025; James et al., 2026; Samaoui et al., 2024; Satti et al., 2026). The spatial correspondence between verified barite occurrences, their host rocks, and structurally disrupted zones suggests that lithological control and structural permeability acted together in localizing mineralization. Accordingly, comparable spectral responses extending beyond the sampled barite exposures are interpreted as expressions of favorable barite-hosting conditions rather than as direct evidence of additional mineralization. Their exploration significance is therefore highest where spectral, lithological, and structural criteria converge.

The integrated lithological–structural map (see Fig. 19) serves as an exploration-oriented geological framework rather than a direct mineral-prospectivity model. Compared to earlier mapping of the study area (Kenea H Nasir, 1997), this approach provides spatially continuous lithological information alongside independently derived spectral and subsurface structural constraints. Its practical value lies in narrowing the reconnaissance search area and prioritizing lithological contacts and structural corridors for subsequent field investigation, rather than replacing conventional geological exploration.

5.5. Limitations and future perspectives

Several limitations must be acknowledged when interpreting the integrated results. Spectral similarity among compositionally related felsic lithologies constitutes a significant source of uncertainty. Granitic, granodioritic, rhyolitic, and felsic metavolcanic rocks often exhibit overlapping quartz–feldspar assemblages. Additionally, weathering, oxidation, hydrothermal alteration, surface coatings, topographic shadowing, and mixed pixels along lithological contacts can further alter their spectral signatures. These factors contribute to the greater class-level confusion observed among certain crystalline units, in contrast to the more distinct Quaternary and wadi deposits.

Variations in spatial and spectral resolution among Landsat, Sentinel-2, ASTER, and PRISMA limit the direct comparison of narrow geological features. As a result, narrow contacts, small lithological bodies, and heterogeneous transition zones may still be influenced by mixed-pixel responses. Since the multispectral, hyperspectral, and gravity datasets were analyzed independently, their integration should be regarded as geological cross-interpretation rather than pixel-level fusion at a consistent spatial resolution.

Field investigations and petrographic analyses of the main rock units and barite samples from the Tehilla–Abu Samar area provide direct evidence for mineralization and its association with felsic metavolcanic host rocks. However, the spatial extent of spectral responses beyond verified exposures remains poorly constrained. Comparable sulfate- and carbonate-sensitive responses may be present in other mineral assemblages, altered surfaces, or weathered materials. Therefore, unsampled extensions of these anomalies should remain exploration targets until further field, mineralogical, and geochemical data are obtained.

Gravity interpretation adds another source of uncertainty. Although GGMplus offers valuable regional information on density contrasts and structural trends, its approximately 7.2 arc-second sampling interval does not correspond to equivalent geological resolution. Potential-field modeling is inherently non-unique, as various combinations of source

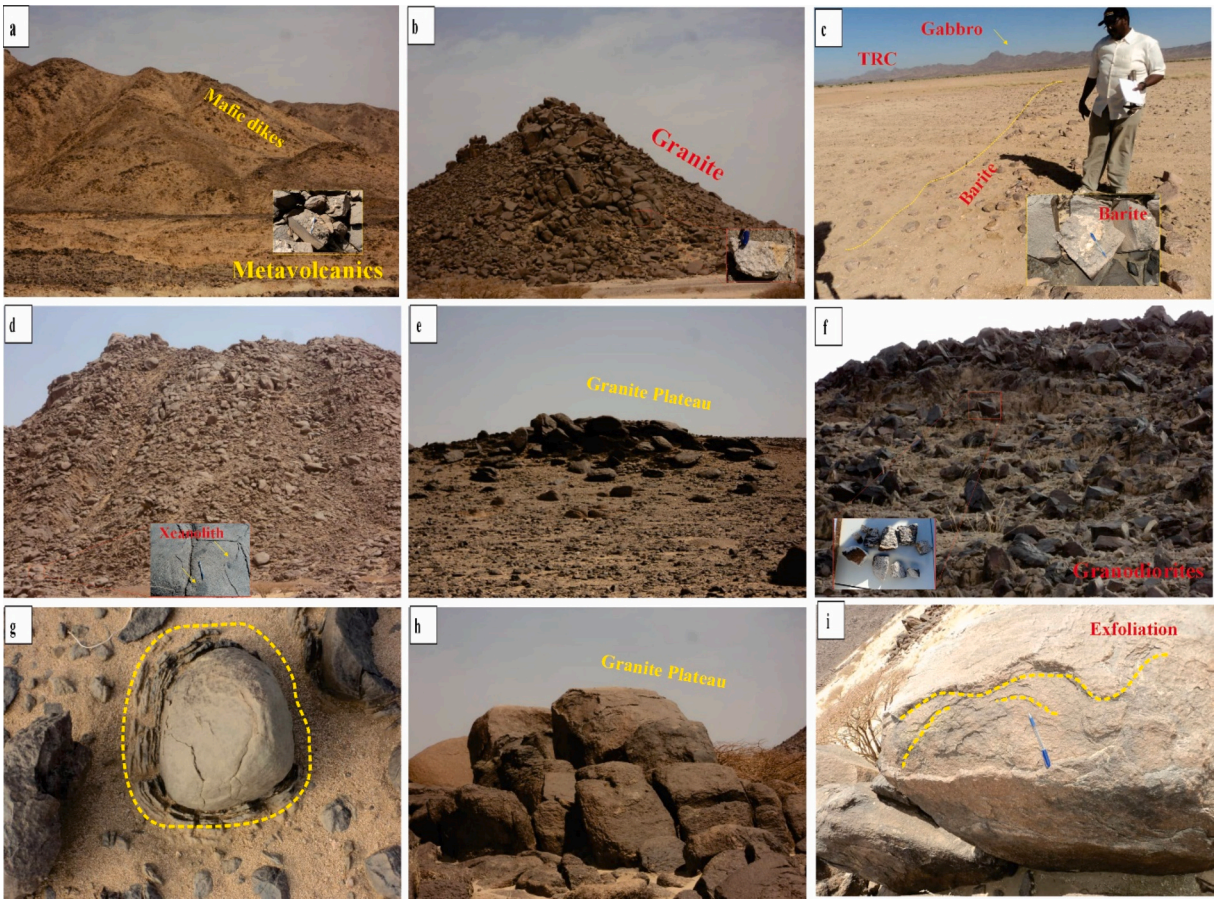


Fig. 20. Field photographs showing representative lithological, structural, and weathering features of the Tehilla–Abu Samar area: (a) altered metavolcanic rocks; (b) granitoid body; (c) the ring-complex landscape with large vein of barite; (d) xenolith-bearing granitoid; (e) granitoid exposure; (f) granodiorite; (g) onion-like weathering of granite; (h) granite plateau; and (i) exfoliation of granitic rocks.

geometry, depth, and density contrast can produce similar anomalies. Additional ground-gravity measurements, especially across the TRC and major shear zones, would provide stronger constraints on the inferred subsurface architecture.

Future research should advance from lithological classification to multisource mineral prospectivity modeling by integrating mapped lithology, alteration-sensitive spectral features, structural parameters, gravity-derived data, field observations, and geochemical indicators within a unified predictive framework. Deep-learning methods should be explored to extract nonlinear spatial and spectral relationships that conventional classifiers may not capture, particularly when high-resolution hyperspectral and multiscale geological datasets are available. Incorporating explainable artificial intelligence, such as SHAP-based feature attribution, would enable quantification and geological interpretation of the relative influence of lithological, spectral, structural, and geochemical predictors on prospectivity estimates. These approaches would be especially valuable for distinguishing statistically favorable targets from geologically significant controls on barite mineralization.

Further improvements should include targeted XRD, SEM–EDS, and major- and trace-element characterization of unsampled priority targets; higher-spatial-resolution hyperspectral observations; increased field control along complex lithological boundaries; and additional ground geophysical surveys. Collectively, these advancements could facilitate the transition from the current integrated lithological–structural framework to a quantitatively validated and geologically interpretable mineral prospectivity model for barite and related mineral systems in the Arabian-Nubian Shield.

6. Conclusion

An integrated lithological and structural framework for the Tehilla–Abu Samar area of the Red Sea Hills was established by combining multispectral and hyperspectral remote sensing, gravity analysis, machine learning-based lithological classification, and field-based geological evidence. This comprehensive approach delineated the principal intrusive, metavolcanic, metasedimentary, and surficial units, thereby providing new constraints on the geological context of the barite mineralization.

Spectral enhancement of Landsat, Sentinel-2, and ASTER data facilitated the characterization of lithological and mineral-sensitive surface variations. In contrast, PRISMA hyperspectral analysis provided more detailed spectral information on compositional variability within the Tehilla Ring Complex and adjacent metavolcanic and metasedimentary successions. The identified hyperspectral endmembers and abundance patterns corresponded with the mapped granitoid, gabbroic, carbonate-bearing, and metavolcanic–metasedimentary domains, offering additional insights for interpreting barite-associated spectral responses.

Machine learning results show that overall performance was closely comparable among XGB, SVM, KNN, and RF, with XGB achieving the highest OA and κ and SVM the marginally highest macro-F1. The consistency among the leading classifiers supports the consistency of the principal lithological framework across the leading classifiers. However, residual confusion among compositionally similar felsic units underscores the terrain's geological and spectral complexity. Gravity analysis provided an independent subsurface constraint, revealing a pronounced anomaly beneath the Tehilla Ring Complex that is consistent with a dense mafic body extending to approximately 5 km depth.

The dominant NE–SW and NW–SE structural trends further delineate major contacts and shear-related corridors, which are key components of geological control on mineralization.

The primary exploration implication is that the most favorable barite targets occur where felsic metavolcanic host rocks, mineral-sensitive spectral responses, documented mineralization, lithological contacts, and major structural corridors intersect. Compared with interpretations based on a single remote sensing or geophysical dataset, this integrated framework provides a more robust foundation for prioritizing exploration targets and guiding subsequent field investigations. Although no formal economic assessment was performed, focusing reconnaissance on geologically favorable zones can improve exploration efficiency and reduce unnecessary field coverage. This framework is applicable to mineral exploration, lithological, and structural investigations of other underexplored Precambrian terrains within the Arabian–Nubian Shield.

CRediT authorship contribution statement

Abazar M.A. Daoud: Writing – original draft, Visualization, Validation, Methodology, Investigation, Data curation, Conceptualization. **Ali A. Mohieldain:** Visualization, Software, Methodology. **Albarra Satti:** Validation, Investigation, Data curation. **Ali Shebl:** Visualization, Validation, Software, Methodology, Data curation. **Richard W. McIntosh:** Writing – review & editing, Visualization, Validation. **Árpad Csámer:** Writing – review & editing, Visualization, Validation. **Péter Rózsa:** Writing – review & editing, Visualization, Validation, Supervision, Resources, Project administration, Funding acquisition.

Declaration of competing interest

The authors declare that they have no known competing financial interests or personal relationships that could have appeared to influence the work reported in this paper.

Acknowledgment

The authors gratefully acknowledge the USGS, the Italian Space Agency (ISA), NASA EarthData, and the GGMplus initiative for providing essential satellite and geospatial datasets. The authors gratefully acknowledge Prof. Dr. Elshiekh M. Abdel Rahman and the Geological Research Authority, Sudan for providing supplementary geochemical data used in this study. This research supported by the University of Debrecen Program for Scientific Publication.

Appendix A

Supplementary data to this article can be found online at https://doi.org/10.1016/j.ejrs.2026.10.001.

References

Abd El-Wahed, M.A., Kamh, S., Attia, M., Eldosouky, A.M., 2025. Structural geometry and gold ores along the first outlined N–S dextral shear zone in the Egyptian Nubian Shield, East African orogenic belt: new insights from integrated remote sensing, gravity, magnetic and field studies. Geomech. Geophys. Geo-Energy Geo-Resour. 11, 76. https://doi.org/10.1007/s40948-025-01003-8.

Abdel Rahman, E.M., 1993. Geochemical and Geotectonic Controls of the Metallogenic Evolution of Selected Ophiolite Complexes from the Sudan. A. Reimer, Selbstverlag Fachbereich Geowissenschaften, FU Berlin.

Abdelkareem, M., Abdalla, F., Yousef, S., 2024. The use of ASTER and landsat remote sensing data for exploring hydrothermal mineral in Arabian-Nubian Shield. Kuwait J. Sci. 51, 100240. https://doi.org/10.1016/j.kjs.2024.100240.

Abdelrahman, K., El-Qassas, R.A.Y., Fnais, M.S., Andráš, P., Eldosouky, A.M., 2023. Geological structures controlling Au/Ba mineralization from aeromagnetic data: Harrat ad Danun area, Saudi Arabia. Minerals 13. https://doi.org/10.3390/min13070866.

Abdelsalam, M.G., 2010. Quantifying 3D post-accretionary tectonic strain in the Arabian-Nubian Shield: Superimposition of the Oko Shear Zone on the Nakasib Suture, Red Sea Hills, Sudan. J. Afr. Earth Sci. 56, 167–178. https://doi.org/10.1016/j.jafrearsci.2009.07.003.

Abdelsalam, M.G., Stern, R.J., 1993. Tectonic evolution of the Nakasib suture, Red Sea Hills, Sudan: evidence for a late Precambrian Wilson cycle. J. Geol. Soc. 150, 393–404. https://doi.org/10.1144/gsjgs.150.2.0393.

Abdelsalam, M.G., Stern, R.J., 1996. Sutures and shear zones in the Arabian-Nubian Shield. J. Afr. Earth Sci. 23, 289–310. https://doi.org/10.1016/S0899-5362(97)00003-1.

Abo Khashaba, S.M., Osman, H., Sami, M., Ahmed, A.F., Zaky, K.S., Hassan, S.M., Drüppel, K., Nagy, M., 2026. Advanced multisource remote sensing and aeromagnetic datasets for lithological discrimination and mineralized zones detection of the El-Sibai area, north Arabian-Nubian Shield. Phys. Chem. of the Earth, Parts A/B/C 144, 104544. https://doi.org/10.1016/j.pce.2026.104544.

Abrams, M., Yamaguchi, Y., 2019. Twenty years of ASTER contributions to lithologic mapping and mineral exploration. Remote Sens. https://doi.org/10.3390/rs11111394.

Abtout, A., Boukerbout, H., Bouyahiaoui, B., Boukercha, F., 2018. Identification of Gravity Lineaments for Water Resources in the Crystalline Massif of Hoggar (South of Algeria). In: Gravity-Geoscience Applications, Industrial Technology and Quantum Aspect. IntechOpen.

Abu-Fatima, M., Marignac, C., Cathelineau, M., Boiron, M.C., 2021. Metallogeny of a Pan-African oceanic arc: VHMS and gold deposits in the Ariab-Arbaat belt, Haya terrane, Red Sea Hills (Sudan). Gondwana Res. 98, 76–106. https://doi.org/10.1016/j.gr.2021.06.001.

Adam, M.S.M., Babikir, K.A., Kim, Y.J., Park, M.E., F.H. Orellana, J., Kim, Y.S., 2024. Geology and structural setting of the undiscovered Amgififa volcanogenic massive sulfide (VMS) deposit in the southwestern part of the Haya terrane, Arabian-Nubian Shield, Sudan. Ore Geol. Rev. 167. https://doi.org/10.1016/j.oregeorev.2024.105969.

Aggarwal, A., Garg, R.D., 2015. Systematic approach towards extracting endmember spectra from hyperspectral image using PPI and SMACC and its evaluation using spectral library. Appl. Geomat. 7, 37–48. https://doi.org/10.1007/s12518-014-0149-5.

Ahmed, F., 1977. Petrology and evolution of the Tehilla igneous complex, Sudan. J. Geol. 85, 331–343. https://doi.org/10.1086/628303.

Alawy, M.K., Abdelwahed, M., Moghazi, A.-K.M., Mohamed, F.H., Khamis, H., Shebl, A., 2025. Utilizing remote sensing and field data for geological mapping and polyphase deformation analysis of um Laseifa ophiolites, Eastern Desert, Egypt. Sci. Rep. 15, 6582. https://doi.org/10.1038/s41598-025-88989-z.

Ali-Bik, M.W., Zafar, T., Hassan, S.M., Sadek, M.F., Abo Khashaba, S.M., 2025. Applications of machine learning algorithms in lithological mapping of Saint Katherine Neoproterozoic rocks in the South Sinai of Egypt using hyperspectral PRISMA data. Sci. Rep. 15, 10192. https://doi.org/10.1038/s41598-025-91963-4.

Arian, H., Alaminia, Z., Ahmadi, H., Pour, A.B., Tabatabaei Manesh, S.M., Lentz, D.R., Parsa, L., 2025. Mapping potential zones of Lithium-bearing pegmatites using ASTER and Sentinel-2 remote sensing imagery in the Tagablor pegmatite Field, Central Afghanistan. Remote Sens. Appl. 38, 101625. https://doi.org/10.1016/j.rsase.2025.101625.

Asghede, K.M., Daoud, A.M.A., Mohammed, M.A.A., Genzebu, W., Kiflay, K.B., Pecsmány, P., Vágó, J., 2025. Development of a litho-structural map for the upper Mereb area, Eritrea, using multi-source remote sensing data and machine learning models. Remote Sens. Appl., 101722 https://doi.org/10.1016/j.rsase.2025.101722.

Askari, G., Pour, A.B., Pradhan, B., Sarfi, M., Nazemnejad, F., 2018. Band ratios matrix transformation (BRMT): a sedimentary lithology mapping approach using ASTER satellite sensor. Sensors 18. https://doi.org/10.3390/s18103213.

Bedini, E., Chen, J., 2020. Application of PRISMA satellite hyperspectral imagery to mineral alteration mapping at cuprite, Nevada, USA. J. Hyperspectral Remote Sensing 10, 87–94. https://doi.org/10.29150/jhrs.v10.2.p87-94.

Bishop, C., Rivard, B., de Souza Filho, C., van der Meer, F., 2018. Geological remote sensing. Int. J. Appl. Earth Obs. Geoinf. https://doi.org/10.1016/j.jag.2017.08.005.

Bosworth, W., Stockli, D.F., 2016. Early magmatism in the greater Red Sea rift: timing and significance. Can. J. Earth Sci. 53, 1158–1176. https://doi.org/10.1139/cjes-2016-0019.

Camacho, M., Alvarez, R., 2021. Geophysical modeling with satellite gravity data: eigen-6C4 vs. GGM Plus. Engineering 13, 690–706. https://doi.org/10.4236/eng.2021.1312050.

Chirico, R., Mondillo, N., Laukamp, C., Mormone, A., Di Martire, D., Novellino, A., Balassone, G., 2023. Mapping hydrothermal and supergene alteration zones associated with carbonate-hosted Zn-pb deposits by using PRISMA satellite imagery supported by field-based hyperspectral data, mineralogical and geochemical analysis. Ore Geol. Rev. 152, 105244. https://doi.org/10.1016/j.oregeorev.2022.105244.

Chouhan, A.K., 2020. Structural fabric over the seismically active Kachchh rift basin, India: insight from world gravity model 2012. Environ. Earth Sci. 79, 316. https://doi.org/10.1007/s12665-020-09068-2.

Clotilde, O., Patrick, A.S., Nfor, N., Daniel, N.J., Theophile, N.M., Rokis, K.P., Dieudonné, B., 2016. Determination of the structural lineaments in the Kribi-campo-ma'an area from a multi-scale analysis of gravity data using the HGM and Euler 3D deconvolution approaches. Int. J. Geosci. 7, 1122–1143. https://doi.org/10.4236/ijg.2016.79085.

Cooley, T., Anderson, G.P., Felde, G.W., Hoke, M.L., Ratkowski, A.J., Chetwynd, J.H., Gardner, J.A., Adler-Golden, S.M., Matthew, M.W., Berk, A., Bernstein, L.S., Acharya, P.K., Miller, D., Lewis, P., 2002. FLAASH, a MODTRAN4-based atmospheric correction algorithm, its application and validation. IEEE International Geoscience and Remote Sensing Symposium. IEEE, pp. 1414–1418. https://doi.org/10.1109/IGARSS.2002.1026134.

Dadi, B., Ouchchen, M., Faik, F., Boutaleb, S., Azzab, D. El, Mamouch, Y., Achkouch, L., Bajadi, A., Abia, E.H., Sadeghi, B., 2024. Hydrothermal fluid pathways and

mineralization potential in the high atlas massif (Morocco) using fuzzy logic and multifractal modeling. Ore Geol. Rev. 175, 106401. https://doi.org/10.1016/j.oregeorev.2024.106401.
Daoud, A.M.A., Shebl, A., Abdelkader, M.M., Mohieldain, A.A., Csámer, Á., Satti, A.M.N., Rózsa, P., 2025. Remote sensing and gravity investigations for barite detection in Neoproterozoic rocks in the Ariab area, Red Sea Hills, Sudan. Remote Sens. Appl. 37. https://doi.org/10.1016/j.rsase.2024.101416.
Di Filippo, M., Mancinelli, P., Cavinato, G.P., Pauselli, C., Sabatini, A., Mirabella, F., De Franco, R., Barchi, M.R., 2025. Bouguer gravity anomaly in the Colfiorito quaternary continental basin, northern Apennines, Central Italy. J. Maps 21. https://doi.org/10.1080/17445647.2025.2503244.
Eldosouky, A.M., El-Qassas, R.A.Y., Pham, L.T., Abdelrahman, K., Alhumimidi, M.S., El Bahrawy, A., Mickus, K., Sehsah, H., 2022. Mapping main structures and related mineralization of the Arabian Shield (Saudi Arabia) using sharp edge detector of transformed gravity data. Minerals 12, 71. https://doi.org/10.3390/min12010071.
Elfadly, M.A., Abdelrady, M., Decarlis, A., Khudeir, A.A., El-Rus, M.A.A., Abbas, H., Hadek, H.H. El, Ibraheem, I.M., Shebl, A., 2026. Multidisciplinary approaches to lithological discrimination and structural mapping for mineral resource assessment. Sci. Rep. 16, 9079. https://doi.org/10.1038/s41598-026-43824-x.
Elkins, T.A., 1951. The second derivative method of gravity interpretation. Geophysics 16, 29–50. https://doi.org/10.1190/1.1437648.
Elsamani, Y., Almuslem, A.A., Tokhi, M. El, 2001. Geology and geotectonic classification of Pan-African gold mineralizations in the Red Sea Hills, Sudan. Int. Geol. Rev. 43, 1117–1128. https://doi.org/10.1080/00206810109465064.
Esmaeili, M., Fathianpour, N., Soltani-Mohammadi, S., 2024. PRISMA hyperspectral imagery for mapping alteration zones associated with Kuhpanj porphyry copper deposit, Southern Iran. European J. Remote Sensing 57. https://doi.org/10.1080/22797254.2023.2299369.
Fawcett, T., 2006. An introduction to ROC analysis. Pattern Recogn. Lett. 27, 861–874. https://doi.org/10.1016/j.patrec.2005.10.010.
Ferreira, Francisco J.F., de Souza, Jeferson, de B. e S. Bongiolo, Alessandra, de Castro, Luís G., 2013. Enhancement of the total horizontal gradient of magnetic anomalies using the tilt angle. Geophysics 78 (3), J33–J41. https://doi.org/10.1190/geo2011-0441.1. https://pubs.geoscienceworld.org/geophysics/article/78/3/J33/300910/Enhancement-of-the-total-horizontal-gradient-of. (Accessed 12 April 2013).
Ghoneim, E., Healey, C., Hemida, M., Shebl, A., Fahil, A., 2023. Integration of geophysical and geospatial techniques to evaluate geothermal energy at Siwa Oasis, Western Desert, Egypt. Remote Sens. 15. https://doi.org/10.3390/rs15215094.
Grauch, V.J.S., Cordell, L., 1987. Short note limitations of determining density or magnetic boundaries from the horizontal gradient of gravity or pseudogravity data. Geophysics. https://doi.org/10.1190/1.1442236.
Grebby, S., Field, E., Tansey, K., 2016. Evaluating the use of an object-based approach to lithological mapping in vegetated terrain. Remote Sens. 8, 843. https://doi.org/10.3390/rs8100843.
Green, A.A., Berman, M., Switzer, P., Craig, M.D., 1988. A transformation for ordering multispectral data in terms of image quality with implications for noise removal. IEEE Trans. Geosci. Remote Sens. 26, 65–74. https://doi.org/10.1109/36.3001.
Gruninger, J.H., Ratkowski, A.J., Hoke, M.L., Shen, S.S., Lewis, P.E., 2004. The sequential maximum angle convex cone (SMACC) endmember model (eds.), p. 1. Doi:. https://doi.org/10.1117/12.543794.
Habashi, J., Jamshid Moghadam, H., Mohammady Oskouei, M., Pour, A.B., Hashim, M., 2024. PRISMA hyperspectral remote sensing data for mapping alteration minerals in Sar-e-Châh-e-Shur region, Birjand, Iran. Remote Sens. 16. https://doi.org/10.3390/rs16071277.
Hamimi, Z., Eldosouky, A.M., Hagag, W., Kamh, S.Z., 2023. Large-scale geological structures of the Egyptian Nubian Shield. Sci. Rep. 13, 1923. https://doi.org/10.1038/s41598-023-29008-x.
Hand, D.J., Till, R.J., 2001. A simple generalisation of the area under the ROC curve for multiple class classification problems. Mach. Learn. 45, 171–186. https://doi.org/10.1023/A:1010920819831.
Harris, J.R., Rogge, D., Hitchcock, R., Ijewliw, O., Wright, D., 2005. Mapping lithology in Canada's Arctic: application of hyperspectral data using the minimum noise fraction transformation and matched filtering. Can. J. Earth Sci. 42, 2173–2193. https://doi.org/10.1139/e05-064.
Heller Pearlshtien, D., Pignatti, S., Greisman-Ran, U., Ben-Dor, E., 2021. PRISMA sensor evaluation: a case study of mineral mapping performance over Makhtesh Ramon, Israel. Int. J. Remote Sens. 42, 5882–5914. https://doi.org/10.1080/01431161.2021.1931541.
Hirt, C., Claessens, S., Fecher, T., Kuhn, M., Pail, R., Rexer, M., 2013. New ultrahigh-resolution picture of earth's gravity field. Geophys. Res. Lett. 40, 4279–4283. https://doi.org/10.1002/grl.50838.
Hubbard, B.E., Gallegos, T.J., Stengel, V., Hoefen, T.M., Kokaly, R.F., Elliott, B., 2024. Hyperspectral (VNIR-SWIR) analysis of roll front uranium host rocks and industrial minerals from Karnes and Live Oak counties, Texas Coastal Plain. J. Geochem. Explor. 257, 107370. https://doi.org/10.1016/j.gexplo.2023.107370.
Ibrahim, W.S., Watanabe, K., Yonezu, K., 2016. Structural and litho-tectonic controls on Neoproterozoic base metal sulfide and gold mineralization in north Hamisana shear zone, south Eastern Desert, Egypt: the integrated field, structural, Landsat 7 ETM+ and ASTER data approach. Ore Geol. Rev. 79, 62–77. https://doi.org/10.1016/j.oregeorev.2016.05.012.
James, M.J., de Oliveira, C.G., Schutesky, M.E., 2026. Zacarias au–(ag–barite) deposit, Neoproterozoic Goiás magmatic arc, Brasília orogen, Central Brazil: constraints on the metallogenesis of a gold-rich quartz–barite exhalite related to volcanogenic massive sulfide mineralization. J. Geol. Soc. Lond. 183. https://doi.org/10.1144/jgs2024-191.
Johnson, C.M., Czamanske, G.K., Lipman, P.W., 1989. Geochemistry of intrusive rocks associated with the Latir volcanic field, New Mexico, and contrasts between evolution of plutonic and volcanic rocks. Contrib. Mineral. Petrol. 103, 90–109. https://doi.org/10.1007/BF00371367.
Johnson, P.R., Abdelsalam, M.G., Stern, R.J., 2003. The Bi'r Umq-Nakasib Suture Zone in the Arabian-Nubian Shield: AKey to Understanding Crustal Growth in the East African Orogen. , International Association for Gondwana Research.
Johnson, P.R., Halverson, G.P., Kusky, T.M., Stern, R.J., Pease, V., 2013. Volcanosedimentary basins in the Arabian-Nubian Shield: markers of repeated exhumation and denudation in a Neoproterozoic accretionary orogen. Geosciences. https://doi.org/10.3390/geosciences3030389.
Kenea, N.H., Ebinger, C.J., Rex, D.C., 2001. Late Oligocene volcanism and extension in the southern Red Sea Hills, Sudan. J. Geol. Soc. 185, 285–294. https://doi.org/10.1144/jgs.158.2.285.
Kokaly, R.F., Clark, R.N., Swayze, G.A., Livo, K.E., Hoefen, T.M., Pearson, N.C., Wise, R.A., Benzel, W., Lowers, H.A., Driscoll, R.L., Klein, A.J., 2017. USGS spectral library version 7. https://doi.org/10.3133/ds1035.
Komadja, G.C., Westman, E., Rana, A., Vitalis, A., 2025. A machine learning approach to lithology classification in mining using measurement while drilling and exploration data. Mining, Metallurgy & Exploration 42, 1955–1973. https://doi.org/10.1007/s42461-025-01286-1.
Kröner, A., Stern, R.J., 2004. Africa: Pan-African orogeny. In: Encyclopedia of Geology. Elsevier Inc., pp. 1–12. https://doi.org/10.1016/B0-12-369396-9/00431-7
Maćkiewicz, A., Ratajczak, W., 1993. Principal components analysis (PCA). Comput. Geosci. 19, 303–342. https://doi.org/10.1016/0098-3004(93)90090-R.
Madani, A.A., Emam, A.A., 2011. SWIR ASTER band ratios for lithological mapping and mineral exploration: a case study from El Hudi area, southeastern desert, Egypt. Arab. J. Geosci. 4, 45–52. https://doi.org/10.1007/s12517-009-0059-8.
Mahboob, M.A., Celik, T., Genc, B., 2024. Predictive modelling of mineral prospectivity using satellite remote sensing and machine learning algorithms. Remote Sens. Appl. 36, 101316. https://doi.org/10.1016/j.rsase.2024.101316.
Mahdi, A.M., Eldosouky, A.M., El Khateeb, S.O., Youssef, A.M., Saad, A.A., 2022. Integration of remote sensing and geophysical data for the extraction of hydrothermal alteration zones and lineaments; Gabal Shilman basement area, Southeastern Desert, Egypt. J. Afr. Earth Sci. 194, 104640. https://doi.org/10.1016/j.jafrearsci.2022.104640.
McNemar, Q., 1947. Note on the sampling error of the difference between correlated proportions or percentages. Psychometrika 12, 153–157. https://doi.org/10.1007/BF02295996.
Mina, M.M.M., Osman, A.A.A., Alnour, M.A.M., Abdalla, R.A.M., Zeinelabdein, K.A.E., Abdelrahman, S., Elawad, H.K.E., Kovács, G., Kiss, G.B., 2025. Remote sensing techniques for mapping hydrothermal alteration zones of volcanogenic massive sulfide deposits in Red Sea Hills, NE Sudan. Egyptian J. Remote Sensing and Space Sci. 28, 280–294. https://doi.org/10.1016/j.ejrs.2025.05.003.
Mohamed Taha, A.M., Liu, G., Chen, Q., Fan, W., Cui, Z., Wu, X., Fang, H., 2024. Toward data-driven mineral prospectivity mapping from remote sensing data using deep Forest predictive model. Nat. Resour. Res. 33, 2407–2431. https://doi.org/10.1007/s11053-024-10387-5.
Nasir, Kenea H., 1997. Digital Enhancement of Landsat Data, Spectral Analysis and GIS Data Integration for Geological Studies of the Derudeb Area, Southern Red Sea Hills, NE Sudan. BERLINER GEOWISSENSCHAFTLICHE ABHANDLUNGEN Reihe D Band 14.
Ninomiya, Y., Fu, B., 2019. Thermal infrared multispectral remote sensing of lithology and mineralogy based on spectral properties of materials. Ore Geol. Rev. https://doi.org/10.1016/j.oregeorev.2018.03.012.
Orynbassarova, E., Ahmadi, H., Pour, A.B., Yerzhankyzy, A., Zakariya, M., Omirzhanova, Z., 2025. PRISMA hyperspectral satellite imagery for mapping alteration minerals and zones in Aktogay porphyry copper deposit, Kazakhstan: implications for new discoveries. Geocarto Int. 40. https://doi.org/10.1080/10106049.2025.2591763.
Pour, A.B., Park, T.Y.S., Park, Y., Hong, J.K., Muslim, A.M., Läufer, A., Crispini, L., Pradhan, B., Zoheir, B., Rahmani, O., Hashim, M., Hossain, M.S., 2019. Landsat-8, advanced spaceborne thermal emission and reflection radiometer, and WorldView-3 multispectral satellite imagery for prospecting copper-gold mineralization in the northeastern Inglefield Mobile Belt (IMB), Northwest Greenland. Remote Sens. 11. https://doi.org/10.3390/rs11202430.
Pour, A.B., Ranjbar, H., Sekandari, M., Abd El-Wahed, M., Hossain, M.S., Hashim, M., Yousefi, M., Zoheir, B., Wambo, J.D.T., Muslim, A.M., 2023. Remote sensing for mineral exploration. In: Geospatial Analysis Applied to Mineral Exploration. Elsevier, pp. 17–149. https://doi.org/10.1016/B978-0-323-95608-6.00002-0.
Pratama, I.P.D., Osawa, T., As-Syakur, A.R., 2023. Identification of fault zone in Bali using GGMPlus gravity and Alos-2 Palsar-2 data. J. Geogr. 15, 46. https://doi.org/10.24114/jg.v15i1.40772.
R Core Team, 2021. R: A Language and Environment for Statistical Computing. R foundation for statistical computing, Vienna, Austria. http://www.r-project.org/.
Rockwell, B.W., Gnesda, W.R., Hofstra, A.H., 2021. Improved automated identification and mapping of Iron Sulfate minerals, other mineral groups, and vegetation using Landsat 8 operational land imager data, San Juan Mountains, Colorado, and Four Corners Region. https://doi.org/10.3133/sim3466.
Rockwell, B.W., Hofstra, A.H., 2008. Identification of quartz and carbonate minerals across northern Nevada using aster thermal infrared emissivity data-implications for geologic mapping and mineral resource investigations in well-studied and frontier areas. Geosphere 4, 218–246. https://doi.org/10.1130/GES00126.1.
Rowan, L.C., Mars, J.C., 2003. Lithologic mapping in the mountain pass, California area using advanced spaceborne thermal emission and reflection radiometer (ASTER)

data. Remote Sens. Environ. 84, 350–366. https://doi.org/10.1016/S0034-4257(02)00127-X.

Sadig, A.A., Ahmed, F., 1989. Gravity signatures over selected ring complexes in the Sudan, and their tectonic significance. J. Afr. Earth Sci. 9, 481–487. https://doi.org/10.1016/0899-5362(89)90032-8.

Samaoui, S., Aabi, A., Boushaba, A., Mohammed, B., Nait Bba, A., Essaifi, A., Baidder, L., Lamrani, O., 2024. Metallogeny and genesis of fault-filling barite-sulfide veins (Ougnat, Morocco): petrography, fluid inclusion, and Sr-S isotopic constraints. Geosciences 14, 83. https://doi.org/10.3390/geosciences14030083.

Satti, A.M.N., ElMakky, A.M., Khalil, K.I., Hassan, M.N.M., Rózsa, P., Daoud, A.M.A., 2026. Mapping and genetic interpretation of VMS-related gossans in the Tagotieb region, Red Sea Hills, NE Sudan using multispectral indices and machine learning models. J. Afr. Earth Sci. 240, 106171. https://doi.org/10.1016/j.jafrearsci.2026.106171.

Semtner, A.-K., Klitzsch, E., 1994. Early Paleozoic paleogeography of the northern Gondwana margin: new evidence for Ordovician-Silurian glaciation. Geol. Rundsch. 83. https://doi.org/10.1007/BF00251072.

Serbouti, I., Raji, M., Hakdaoui, M., 2022. Lithological mapping for a semi-arid area using GEOBIA and PBIA machine learning approaches with Sentinel-2 imagery: case study of Skhour Rehamna, Morocco, pp. 143–156. https://doi.org/10.1007/978-3-030-80458-9_11.

Shackleton, R.M., 1994. Review of late Proterozoic sutures, ophiolitic melanges and tectonics of eastern Egypt and north-East Sudan. Geol. Rundsch. 83, 537–546. https://doi.org/10.1007/BF01083226.

Shang, C.K., Morteani, G., Satir, M., Taubald, H., 2010. Neoproterozoic continental growth prior to Gondwana assembly: constraints from zircon-titanite geochronology, geochemistry and petrography of ring complex granitoids, Sudan. Lithos 118, 61–81. https://doi.org/10.1016/j.lithos.2010.03.015.

Shebl, A., Abriha, D., Dawoud, M., Ali Hussein Ali, M., Csámer, Á., 2024. PRISMA vs. Landsat 9 in lithological mapping – a K-fold cross-validation implementation with random Forest. Egypt. J. Remote Sens. Space Sci. 27, 577–596. https://doi.org/10.1016/j.ejrs.2024.07.003.

Sorrentino, A., Chirico, R., Corrado, F., Laukamp, C., Di Martire, D., Mondillo, N., 2024. The application of PRISMA hyperspectral satellite imagery in the delineation of distinct hydrothermal alteration zones in the Chilean Andes: the Marimaca IOCG and the Río Blanco-Los Bronces cu-Mo porphyry districts. Ore Geol. Rev. 167. https://doi.org/10.1016/j.oregeorev.2024.105998.

Stern, R.J., Abdelsalam, M.G., 1998. Formation of juvenile continental crust in the Arabian Nubian shield: evidence from granitic rocks of the Nakasib suture, NE Sudan. Geol. Rundsch. 87, 150–160. https://doi.org/10.1007/s005310050196.

Stern, R.J., Johnson, P.R., 2018. Constraining the opening of the red sea: Evidence from the neoproterozoic margins and cenozoic magmatism for a volcanic rifted margin. In: Geological Setting, Palaeoenvironment and Archaeology of the Red Sea. Springer International Publishing, pp. 53–79. https://doi.org/10.1007/978-3-319-99408-6_4.

Stern, R.J., Johnson, P.R., Kröner, A., Yibas, B., 2004. Neoproterozoic ophiolites of the Arabian-Nubian Shield. Developments in Precambrian Geology. https://doi.org/10.1016/S0166-2635(04)13003-X.

Tripathi, P., Garg, R.D., 2020. First impressions from the PRISMA hyperspectral Mission. Curr. Sci. 119, 1267. https://doi.org/10.18520/cs/v119/i8/1267-1281.

Vail, J.R., 1985. Alkaline ring complexes in Sudan. J. African Earth Sci. (1983) 3, 51–59. https://doi.org/10.1016/0899-5362(85)90022-3.

Vail, J.R., 1988. Lexicon of geological terms for the Sudan. Routledge, London. https://doi.org/10.1201/9780203749036.

Van der Meer, F.D., van der Werff, H.M.A., van Ruitenbeek, F.J.A., 2014. Potential of ESA'S Sentinel-2 for geological applications. Remote Sens. Environ. 148, 124–133. https://doi.org/10.1016/j.rse.2014.03.022.

Van der Meer, F.D., Van der Werff, H.M.A., Van Ruitenbeek, F.J.A., Hecker, C.A., Bakker, W.H., Noomen, M.F., Van der Meijde, M., Carranza, E.J.M., de Smeth, J.B., Woldai, T., 2012. Multi- and hyperspectral geologic remote sensing: a review. Int. J. Appl. Earth Obs. Geoinf. https://doi.org/10.1016/j.jag.2011.08.002.

van der Werff, H., van der Meer, F., 2015. Sentinel-2 for mapping iron absorption feature parameters. Remote Sens. 7, 12635–12653. https://doi.org/10.3390/rs71012635.

Wipfler, E.L., 1996. Transpressive structures in the Neoproterozoic Ariab-Nakasib Belt, Northeast Sudan: evidence for suturing by oblique collision. J. Afr. Earth Sci. 23, 347–362. https://doi.org/10.1016/S0899-5362(97)00006-7.

Younis, M.A., Elyaseer, M.H., Shahin, T.M., El-Desoky, H.M., 2025. Integrated remote sensing and petrological study of garnet-bearing rocks in the Arabian-Nubian shield: a case study from Wadi Shait-Wadi Gemal area, south Eastern Desert, Egypt. Sci. Rep. 15, 35409. https://doi.org/10.1038/s41598-025-21601-6.

Younis, M.T., Gilabert, M.A., Melia, J., Bastida, J., 1997. Weathering process effects on spectral reflectance of rocks in a semi-arid environment. Int. J. Remote Sens. 18, 3361–3377. https://doi.org/10.1080/014311697216928.

Yuan, M., Li, Q., Zhang, B., Pan, J., Gao, L., Jing, L., Lu, L., 2026. A systematic review of deep learning methods for mineral exploration using multisource geoscience data (2018–2025). Int. J. Appl. Earth Obs. Geoinf. 149, 105254. https://doi.org/10.1016/j.jag.2026.105254.